iScience

CellPress
OPEN ACCESS

Article

Anatomical organization of temporally correlated neural calcium activity in the hippocampal CA1 region

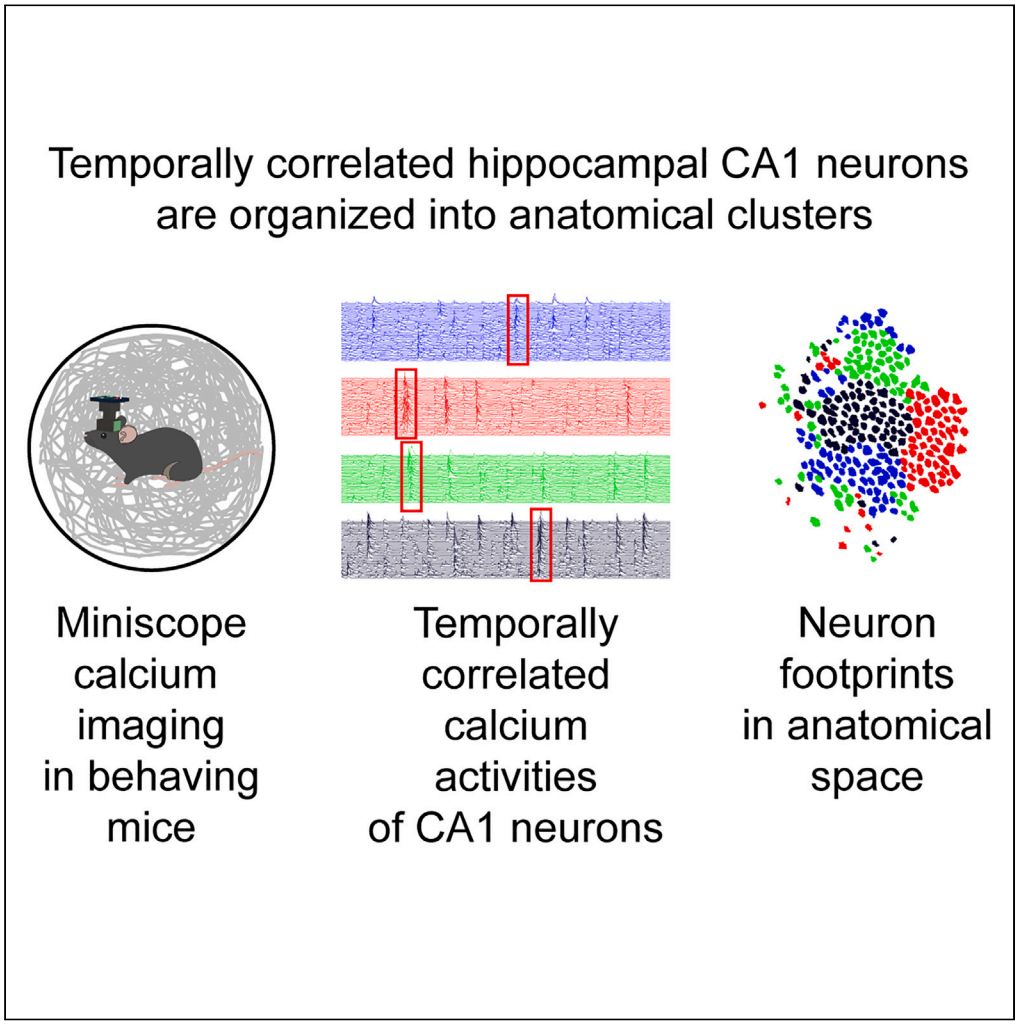

Lujia Chen, Xiaoxiao Lin, Qiao Ye, Zoran Nenadic, Todd C. Holmes, Douglas A. Nitz, Xiangmin Xu

dnitz@ucsd.edu (D.A.N.)
xiangmix@uci.edu (X.X.)

Highlights

Temporally correlated CA1 pyramidal cells are organized into anatomical clusters

Ensemble activities of intra-cluster cells cover different regions of environment

Anatomical clusters reorganize during obvious environment change

Anatomical clusters continue to exist during immobility in a dark environment

Chen et al., iScience 26, 106703
May 19, 2023
https://doi.org/10.1016/j.isci.2023.106703

iScience

CellPress
OPEN ACCESS

Article

Anatomical organization of temporally correlated neural calcium activity in the hippocampal CA1 region

Lujia Chen,[1,4,7,8] Xiaoxiao Lin,[1,7,8] Qiao Ye,[1,4,7] Zoran Nenadic,[4,7] Todd C. Holmes,[2,7] Douglas A. Nitz,[3,7,*] and Xiangmin Xu[1,4,5,6,7,9,*]

SUMMARY

Hippocampal CA1 neuronal ensembles generate sequential patterns of firing activity that contribute to episodic memory formation and spatial cognition. Here we used *in vivo* calcium imaging to record neural ensemble activities in mouse hippocampal CA1 and identified CA1 excitatory neuron sub-populations whose members are active across the same second-long period of time. We identified groups of hippocampal neurons sharing temporally correlated neural calcium activity during behavioral exploration and found that they also organized as clusters in anatomical space. Such clusters vary in membership and activity dynamics with respect to movement in different environments, but also appear during immobility in the dark suggesting an internal dynamic. The strong covariance between dynamics and anatomical location within the CA1 sub-region reveals a previously unrecognized form of topographic representation in hippocampus that may guide generation of hippocampal sequences across time and therefore organize the content of episodic memory.

INTRODUCTION

Hippocampal CA1 neurons are well-known for the spatial tuning of their dynamics within the boundaries of the observable environment.[1–3] Because their spatially specific firing fields are approximately uniform in their environmental distribution, ensembles of "place cells" are activated in sequential patterns depending on the trajectories the animal takes through an environment.[4–7] The compression and recurrence of such sequences within each cycle (~125 ms) of locomotion-driven theta-frequency oscillation yield a set of highly organized spike-timing relationships among interconnected hippocampal neurons.[4,7,8] Such sequencing is thought to be consequential with respect to the generation of episodic memories.[4,8]

The "place-specific" firing of hippocampal neurons over longer, seconds-duration time periods can also be systematically matched to the specific trajectories taken through any given environment.[9–16] Notably, trajectory shape can promote the generation of path-discernable sequences for different visits to a single location.[9,10,12–15,17,18] Brain dynamics promoting synaptic potentiation according to activity patterns at this second-long timescale have also been identified.[19]

Multiple factors contribute to the organization of path-specific sequential patterns of CA1 neuron activity. Sequences in hippocampal sub-region CA1 are thought to be generated, at least in part, by connectivity motifs within highly "auto-associative" sub-regions such as CA3[20–24] and the distinct axonal arborization patterns of GABAergic interneurons.[25–27] Such "internal" connectivity constraints molding CA1 firing patterns are thought to interact with inputs coding for relation to distal visual cues, proximity to boundaries, self-motion cues, heading direction, and trajectory in regions such as the medial entorhinal cortex and nucleus reuniens.[12,28–32] Yet, similar sequential patterns of CA1 neuron activity can be observed even under conditions of minimal sensory input in immobile and sleeping animals.[33] These firing patterns are thought to represent internal dynamics of mental replay of previously learned routes and highlight both the constrained and versatile nature of CA1 neurons regarding their specific sequential patterns of activity.

Due to the complexity of factors influencing CA1 neuron firing, including restrictions on the scope of activity measurements, few studies have asked whether the temporal dynamics of CA1 neurons are related to

[1]Department of Anatomy and Neurobiology, School of Medicine, University of California, Irvine, Irvine, CA 92697-1275, USA

[2]Department of Physiology and Biophysics, School of Medicine, University of California, Irvine, Irvine, CA 92697- 4560, USA

[3]Department of Cognitive Science, University of California, La Jolla, La Jolla, CA 92093, San Diego

[4]Department of Biomedical Engineering, University of California, Irvine, Irvine, CA 92697-2715, USA

[5]Department of Microbiology and Molecular Genetics, University of California, Irvine, Irvine, CA 92697-4025, USA

[6]Department of Computer Science, University of California, Irvine, Irvine, CA 92697-3435, USA

[7]The Center for Neural Circuit Mapping, University of California, Irvine, Irvine, CA 92697, USA

[8]These authors contributed equally

[9]Lead contact

*Correspondence: dnitz@ucsd.edu (D.A.N.), xiangmix@uci.edu (X.X.)

https://doi.org/10.1016/j.isci.2023.106703

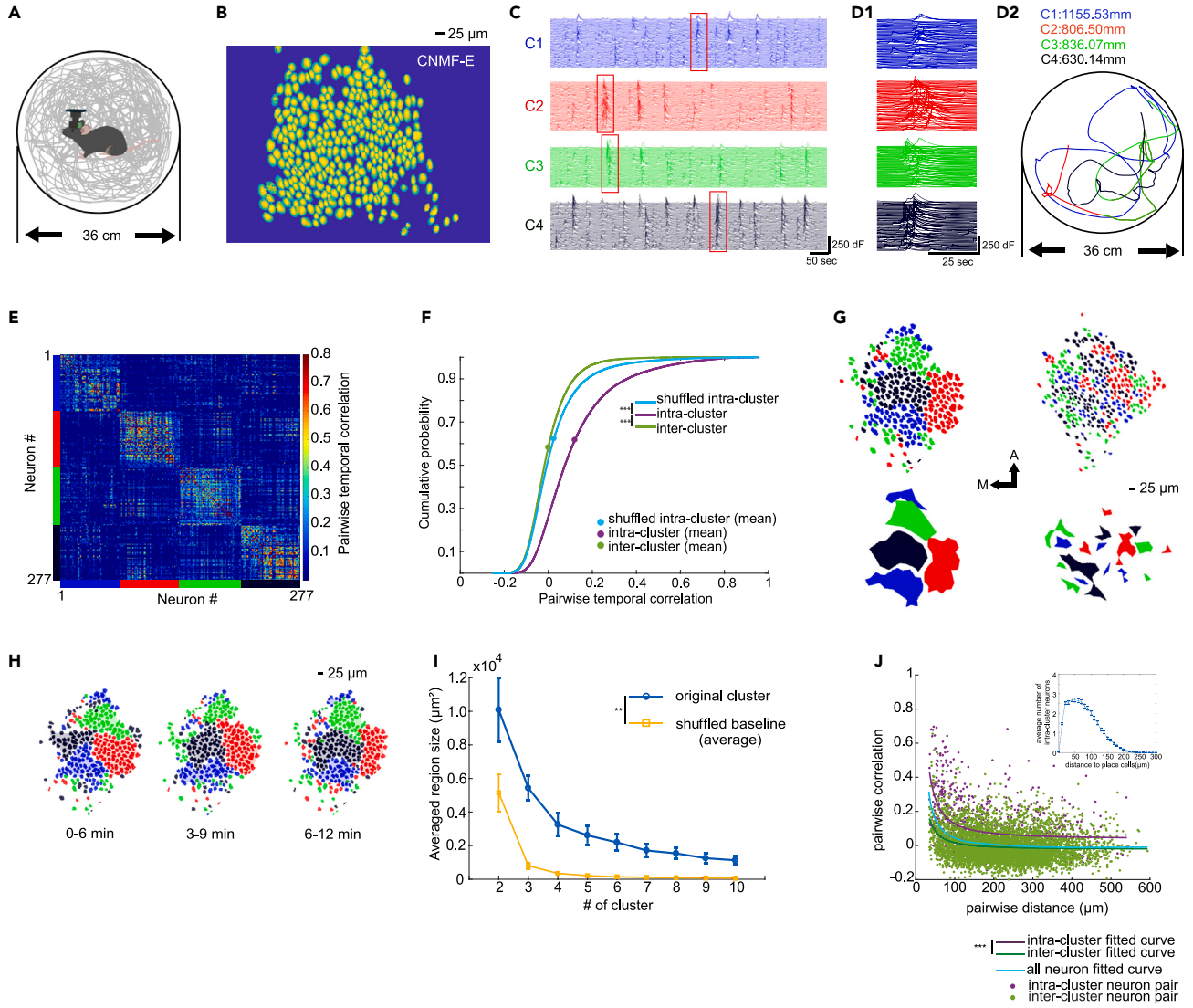

Figure 1. Hippocampal CA1 neurons are organized into anatomically clustered groups with temporally correlated calcium activities

(A) Illustration of a mouse with a head-mounted miniscope targeting the hippocampal CA1 region, and the behavioral arena (36 cm diameter circle box) in which the mouse can freely explore with simultaneous calcium event neural imaging. Gray line indicates the trajectory of one example mice exploring for 12 min.

(B) Illustration of neuron footprints extracted by CNMF-E during the processing of miniscope imaging data. The scale bar represents 25 μm.

(C) Temporal calcium traces of all neurons grouped into clusters recorded from a single mouse (C1-C4). The vertical scale bar represents a unit of 250 dF of calcium signal changes; the horizontal scale bar represents 50 seconds in time.

(D1) Magnification of the red boxed areas in C. The aligned calcium events are clearly seen in the magnified trace segment. The vertical scale bar represents 250 dF; the horizontal scale bar represents 25 seconds.

(D2) Trajectories corresponding to the four magnified calcium event segments presented in d (trajectory length: C1: 1155.53 mm, C2: 806.50 mm, C3: 836.07 mm, C4: 630.14 mm).

(E) Pairwise temporal correlation matrix. Both axes represent neuron indexes which are grouped by clusters.

(F) Comparisons of cumulative probabilities between intra- and inter-cluster pairwise temporal correlations of neuron calcium event dynamics, as well as shuffled intra-cluster pairwise correlation. Intra-cluster correlation is significantly higher than both shuffled and inter-cluster correlation (intra-cluster, 0.1206 $\pm$ 0.0006; inter-cluster, 0.0031 $\pm$ 0.0006; shuffled intra-cluster, 0.0202 $\pm$ 0.0006; intra-cluster versus inter-cluster, p = $1.0257*10^{-40}$, intra-cluster versus shuffled intra-cluster-cluster, p = $4.1659*10^{-24}$, two sample Kolmogorov-Smirnov test, Data are presented as the mean $\pm$ SEM).

(G) Anatomical clusters of neural calcium event footprints from temporally correlated neurons. Two example mice are shown here. The scale bar represents 25 μm. For the anatomical axis symbols, A refers to anterior and M refers to medial.

(H) Anatomical cluster changes during 3 semi-overlapping epochs of a single recording session for the example mouse in G (the left one). The scale bar represents 25 μm.

Figure 1. *Continued*

(I) Averaged patch size of anatomical clusters across different cluster numbers. Error bars represent the SEM of patch sizes across six mice perform the same task at the specific cluster number. Blue circle: Patch size of the original anatomical clusters. Yellow square: average size of the shuffled cluster patches serves as shuffled baseline (Original cluster patch size curve v.s. shuffled baseline curve: $p = 0.0039$, Wilcoxon matched pairs signed rank test, $N = 9$ cluster numbers).

(J) Relationship between pairwise temporal correlations and pairwise anatomical distance of neuron pairs. Intra- and inter-cluster data is represented as purple and green, respectively. The distribution of intra- and inter-cluster data is fitted to a first-order power function. Overall, for all the mice, across neuron pairs with different pairwise distances, a significant negative relationship is identified between pairwise temporal correlation and pairwise distance (Cyan line, spearman correlation = −0.1976, $p = 3.9975*10^{-67}$). Also, across neuron pairs with different pairwise distances, the pairwise temporal correlation of intra-cluster neuron pairs is significantly higher than that of inter-cluster neuron pairs ($p = 3.8966*10^{-18}$, Wilcoxon matched pair signed rank test, $N = 100$ distance levels). The subplot on the right top illustrates the distribution of neighboring cells toward intra-cluster place cells. Asterisks are defined as $p \leq 0.05$ *, $p < 0.01$ **, $p < 0.001$ ***. See also Figure S3.

their anatomical distribution.[34] Such a relationship would reveal a hippocampal organization that has previously eluded experimenters. In the present work, we have directly addressed this question by examining the temporal dynamics of large numbers of CA1 neurons longitudinally using *in vivo* calcium imaging with miniature head-mounted microscopes ("miniscopes") in mice during free exploration of multiple environments. We identify groups of CA1 neurons with temporally correlated calcium activity patterns and find that these groups are organized anatomically within CA1. This reveals a previously unrecognized form of topographic representation in the hippocampus that may guide neural activity contributing to spatial navigation and episodic memory.

RESULTS

Anatomical clustering of temporally correlated neurons

To determine whether the temporally correlated activity of CA1 neurons is related to their anatomical distribution in the hippocampus, we employed the miniscope imaging of Ca^{++} transients (Figure S1) while mice freely explored one of the several environments of different shapes and bearing different sets of boundary wall visual cues (Figures 1A and 1B). Using the K-means-based consensus clustering algorithm (KCC) that categorizes neurons based on temporal correlation,[35] we determine that CA1 does indeed exhibit neuron sub-populations activated in sequences spanning several seconds ($n = 6$ mice). Notably, the sub-populations identified by this method contain many members whose activations are not strictly synchronous or even overlapping in time but nevertheless, fall within the same multi-second windows of time. We observe a strong correlation of neuron-neuron activity vectors within each group and a relatively weak correlation of activity across groups (Figures 1C and 1D). Temporally correlated activity among members of each group occurs over periods of greater than 3 s, approximately following the time frame identified in recent work that measured synaptic potentiation among neurons active within a few seconds of each other.[19] The periods of correlated activation can cover large behavioral movement trajectories in the arena up to >110 cm (Figure 1D2).

We then graphed neuron-neuron temporal correlations among all pairs recorded during arena exploration. By organizing the X and Y axes of the correlation matrix according to group identity, neurons of the same group (intra-cluster, Figure 1E) exhibit higher correlations with each other than with neurons from different groups (inter-cluster, Figure 1E). To determine statistical significance, we constructed cumulative probability functions for all the pairwise correlations between neurons as shown in Figure 1F. The cumulative probability functions for neuron pairs from the same group (purple curve), from different groups (green curve), and after random shuffling of group identities (blue curve) are depicted. Neuron pairs from the same group exhibit significantly higher correlations than when group identities are randomized, and when neurons in pair are not from the same group (Figure 1F). These results further illustrate that the CA1 pyramidal neurons can be organized into distinct groups based on the temporal correlations in their activity.

Having established CA1 neuron group identity based on temporal activity profiles, we then asked whether these groupings exhibit any specific anatomical distributions. To address this, we visualized the anatomical profile of neurons from each temporal cluster across the imaged sub-region of CA1. Strikingly, this reveals that temporally correlated neurons are clustered anatomically into irregularly shaped patches (Figure 1G, left, right for two different example cases). Within such groupings, any given pair of neurons may reside next to each other or be hundreds of microns apart; nevertheless, the members of each group cover one or more contiguous patches of CA1 anatomical space. To test the stability of anatomical clustering

across the exploration session, we divided the recording session into several epochs and visualized the distribution of neurons from each temporal grouping in an anatomical map. While CA1 neuron activation across a given space may vary significantly as a function of time, trajectory, or behavior,[36,37] we found the anatomical clustering defined by temporal correlation exhibit a higher-than-expected level of stability throughout the duration of the recording session, that among all possible pairs of neurons, on average around 35%-40% of pairs stay in the same cluster across different periods of recording session (Figures 1H and S3J).

We measured the spatial span of anatomical clustering of temporally correlated neurons using density-based spatial clustering of applications with noise (DBSCAN). This algorithm de-noises and defines contiguous populations of individual elements and their boundaries[38] (see Figure 1G, lower panels, which show defined contiguous regions; see Figure S2 for a description of the method). Across mice, detected contiguous patches have an average area of ~2000 μm^2 over the topographical surface of CA1. In addition, we also observe that anatomical clusters formed by temporally correlated neurons are not always present as one contiguous region. Smaller islands can sometimes be found isolated from the major region, a characteristic we refer to as fractured domain topography.

We then asked whether our clustering algorithm, and the choice of cluster numbers, affect the detected patches. To address this, we first compared the original patch size across mice (i.e., patch size determined by temporally detected clusters), with their corresponding shuffled baseline (i.e., patch size determined by the same data with cluster identities randomized). We found the patch size of original clusters significantly surpass the shuffled baseline (Figure S3N. See Figure S3O for another arena). We then compared the patch size across different cluster numbers, as shown in Figure 1 I, where the patch size of original anatomical clusters significantly exceeds the patch sizes of clusters with randomized identities. (See further examples from a different arena in Figure S3G). We also utilized an independent component analysis (ICA)-based algorithm[39] to examine if our observation is brought by our k-mean based clustering algorithm itself, and find that ICA-based algorithm also picked up both the temporal and anatomical clusters we described previously (Figure S10), which indicate the results described here is not induced by the clustering algorithm itself. The above analysis shows neither the clustering algorithm, nor the number of clusters chosen, has a significant effect in the notability of patches, and that the detected contiguous CA1 patches should be physiologically meaningful.

A potential concern regarding the detected anatomical clusters is that the viral transfection approach we applied may cause unhealthy physiological conditions due to the cellular toxicity of potential viral overexpression. To address this issue, we first examined the histology and morphology of neurons with immunostaining (Figure S1). Overall, we do not note CA1 pyramidal neurons exhibiting aberrant shapes which indicate unhealthy conditions. We also checked the length / duration of transients for the virus infected mice used in the experiment (Figure S8) and find the most concentrated transient length is around 2-3 s, which follows the descriptions of previous studies.[40] Finally, we also applied the same cluster detection technique to a group of 5 Camk2a-Cre; Ai163 mice performing free exploration inside an open square arena. The Ai163[41] strain is a Cre-dependent calcium inicator expressing mouse line, which has been found to be less volunerable to toxicity issues when used in conjunction with the Camk2a-Cre strain. As shown in Figures S3I-S9E, Camk2a-Cre; Ai163 mice have CA1 excitatory cell clusters that display visually distinguishable anatomical regions that are larger than shuffled baseline across all the potential cluster number candidates. It is noted that the identified anatomical clusters are more fractured in the transgenic mouse cases, which is likely due to less dense transgenic GCaMP expression in CA1 excitatory cells compared with AAV transduction (Figure S9). Based on the contents above, we conclude the anatomical clustering of CA1 excitatory cells is unlikely to be induced by virus toxicity.

A second question concerns the potential signal overlap of imaged neural activity between neighboring neurons. To address this, we compared the correlation of neighboring intra- and inter-cluster neurons at the border of each cluster, for mice from different experiments. If the formation of anatomical clusters is dominated by neighboring neuron interference, the pairwise correlation distribution of neighboring inter-cluster neurons should not be distinguishable from that of neighboring intra-cluster neurons. However, we find that even at the border, neighboring inter-cluster neuron pairs have a significantly lower correlation than border intra-cluster or any intra-cluster neighboring neuron pairs (Figure S11). This provides additional evidence that signal overlap cannot explain the formation of the anatomical contiguous patches illustrated here.

Finally, a third potential confound lies in the possibility that dendritic signals may contaminate the recorded data and give rise to the correlated neighboring components. We first note that this explanation of the data is not consistent with the differences between intra-cluster and extra-cluster pairs at the border between clusters. Nevertheless, we also addressed this concern by utilizing an additional CNMF-E's dendrite detection feature, which can include detected components to be a variety of shapes rather than only ellipse shapes that are considered as typical for soma. We compared the neuron extraction result with the dendrite detection feature being turned on or off and found little difference between the two kinds of extraction (Figure S14). The imaged data contains mostly ellipse-shaped components which are predominantly cell soma. We also checked the number of firing fields our detected neurons displayed in the experiments (Figure S16). Overall, a high percentage of neurons have two or less fields (~75%), indicating that our results are not dominated by components with highly dispersed firing profile.

We also utilized a recently published algorithm, TUnCaT, to unmix and remove the background and dendritic influence from the detected neuron traces[42] and examined the effect on cluster detection in six example mice with virus-induced GCaMP expression. Comparing the CMNF-E extracted trace and the TUnCaT extracted trace, we note that although most above-threshold peak activities are aligned, some only exist in CNMF-E or TUnCaT traces (Figure S17B). We, therefore, quantified the difference between the total above-threshold peak numbers for the original CNMF-E extracted calcium trace and the TUnCaT extracted calcium traces. Overall, across the six mice, the majority of neurons (~90%) have a calcium transient peak number difference ≤ 22 for a duration of 10 min of recording, while ~50% of the neurons have a peak number difference ≤ 5 (Figure S17C). Further, we performed cluster detection using the TUnCaT-generated calcium traces and examined the patch size of the observed anatomical clusters. We compared the averaged patch size with its corresponding shuffled baseline across different cluster numbers. Similar to CNMF-E detected clusters, the patch sizes of anatomical clusters generated with TUnCaT processed calcium traces significantly exceed the patch sizes of randomized baseline. (Figure S17E).

Two-photon microscopy distinguishes neuronal and non-neuronal structures. Existing 2-photon studies have provided various views on the anatomical organizations of CA1 neurons discussed above. Modi et al.[34] found similar anatomical contiguous patches that resemble our results after a trace-eyeblink learning task. Dombeck et al.[43] showed a negative relationship between CA1 pyramidal cell pairwise distance and pairwise correlation when including all neurons in the field of view. While 2-photon calcium imaging is difficult to apply in freely moving mice, we attempted to follow Dombeck et al.'s analysis approach by directly examining the relationship between temporal correlation and distance of recorded principal neuron pairs that have pairwise distances beyond 35 μm for this analysis.[43] We found that overall, CA1 principal neuron pairs across mice display a negative relationship between pairwise distance and temporal correlation (Figure 1J cyan line, spearman correlation = −0.1976). This result is consistent with Dombeck et al.'s result that includes all neurons in view. It should be noted though, that Dombeck et al.'s analytical approach is qualitatively different from our clustering analysis, and may underestimate anatomical clustering because here, any two neurons assigned to the same cluster can be neighboring or distant from each other.

We further examined the distribution of pairwise correlations for intra- and inter-cluster neuron pairs over different distances (Figure 1J, green and purple line). Both intra- and inter-cluster neuron pairs show similar correlation-distance relationships compared to the overall trend. Using the fit curves of intra-cluster and inter-cluster correlation-distance distributions, we find that across a wide range of distance levels, intra-cluster cell pairs exhibit higher pairwise correlation compared to that of inter-cluster cell pairs ($p = 3.8966*10^{-18}$, Wilcoxon matched pair signed rank test). This is consistent with the observation that members of a temporally correlated neural cluster can go into multiple anatomically contiguous spaces that are either in proximity or hundreds of microns apart. Meanwhile, consider the results in Figure S11, two directly neighboring neurons can be of the same or different clusters, and their temporal correlations will tend to be high and low, respectively. We note here and elsewhere that the form of topographic representation seen in our data differs in character from that tested for in some prior studies.[44,45] In those studies, the tested model most often assumes that all neighboring neurons should have location-specific firing fields in close proximity to each other, and that neurons at further distances from each other should have proportionally distributed distances between their location-specific firing field centers. This model is derived according to the correlation in location-specific firing activity of hippocampal neurons as opposed to the temporal correlation approach utilized here. The latter and current approach can yield

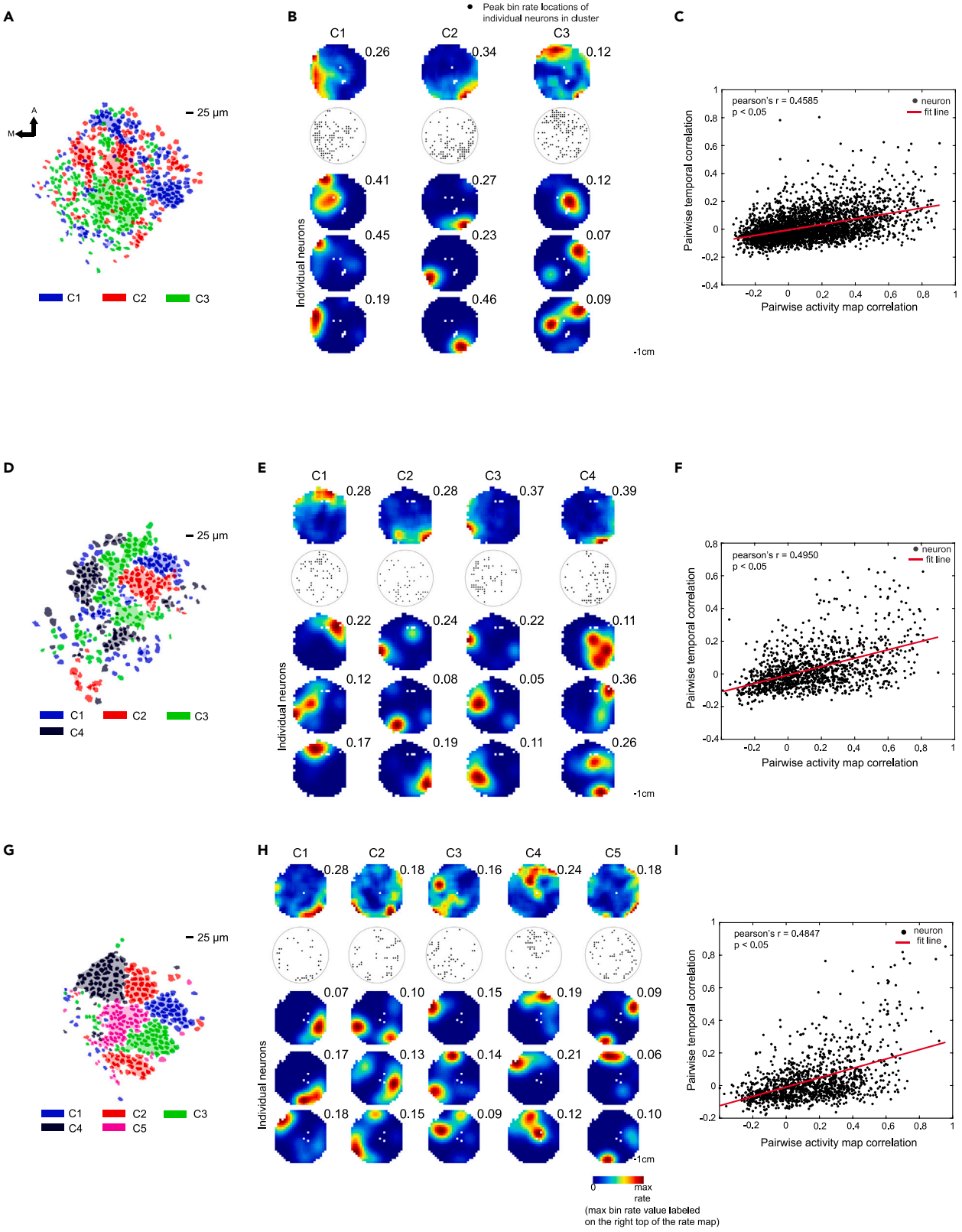
A
25 μm
C1
C2
C3
B
Peak bin rate locations of individual neurons in cluster
C1
C2
C3
0.26
0.34
0.12
0.41
0.27
0.12
0.45
0.23
0.07
0.19
0.46
0.09
Individual neurons
1cm
C
pearson's r = 0.4585
p < 0.05
neuron
fit line
Pairwise temporal correlation
Pairwise activity map correlation
D
25 μm
C1
C2
C3
C4
E
C1
C2
C3
C4
0.28
0.28
0.37
0.39
0.22
0.24
0.22
0.11
0.12
0.08
0.05
0.36
0.17
0.19
0.11
0.26
Individual neurons
1cm
F
pearson's r = 0.4950
p < 0.05
neuron
fit line
Pairwise temporal correlation
Pairwise activity map correlation
G
25 μm
C1
C2
C3
C4
C5
H
C1
C2
C3
C4
C5
0.28
0.18
0.16
0.24
0.18
0.07
0.10
0.15
0.19
0.09
0.17
0.13
0.14
0.21
0.06
0.18
0.15
0.09
0.12
0.10
Individual neurons
1cm
0
max rate
(max bin rate value labeled on the right top of the rate map)
I
pearson's r = 0.4847
p < 0.05
neuron
fit line
Pairwise temporal correlation
Pairwise activity map correlation

Figure 2. Anatomical clusters are the basis of the functional organization during the exploration of different regions of the behavioral arena

(A, D, G) Anatomical clusters for three representative mice imaged while freely exploring an identical behavioral arena. The scale bar represents 25 μm. For the anatomical axis symbols, A refers to anterior and M refers to medial.

(B, E, H) Upper portion of the panels represents ensemble activity maps of the anatomical clusters in A, E, I. Black dots represent the maximal activity location of individual intra-cluster neurons. Lower portion of the panels represents activity maps of 3 representative neurons from each anatomical cluster. The number on the right top of each activity map represents the maximum bin rate in the map. For all activity maps, each bin represents 1 cm*1 cm of the arena space.

(C, F, I) Relationship between pairwise temporal correlation and pairwise activity map correlation for neuron pairs within the anatomical clusters for the three representative mice depicted in A, E, and I. Each of the neuron pairs is represented by a single black dot. For all 3 example mice, the pairwise temporal correlations have significant linear relationship with pairwise activity map correlation (mouse1: Pearson's r = 0.4585, p = $6.1241*10^{-68}$; mouse 2: Pearson's r = 0.4950, p = $2.6525*10^{-33}$; mouse 3: Pearson's r = 0.4847, p = $1.8400*10^{-31}$). See also Figures S5, S6, S7, S12, and S13.

correlations that partially depend on location-specific activity but also allows the specific trajectories through space to define different temporal sequences of activity.

Furthermore, a recent study reported synchronized firing of neighboring CA1 pyramidal neurons after the artificial activation of a "seed" CA1 pyramidal neuron using 2-photon microscopy. These synchronized neurons have a high spatial concentration around 50-100 μm range relative to the seed neurons.[43] We, therefore, calculated the number of intra-cluster neurons of different distances toward intra-cluster place cells. We used a conservative method to define "place cells" according to the quantification of firing activity maps with the metrics coherence and spatial information/event. Spatial information/event measures the feature of the distribution in firing rates across environmental locations; values for this measure are high when a small proportion of spatial bins are associated with high activity across a much larger background of inactivity. Coherence complements this measure in reflecting the tendency for high-activity spatial bins to be neighboring, as one would expect for a place field. We found that on average, to each place cell the number of neighboring intra-cluster neurons display a similar cell number-distance trend as noted by Geiller et al.[46] (Figure 1 J right top panel, see Figure S4 for the anatomical distribution of place cells). This further supports the anatomical organization we describe here.

Anatomical clustering and its relation to location-specific firing

As considered briefly in the preceding section, an important question here concerns how location-specific activity of CA1 cells relates to the identified anatomical distribution of temporally correlated CA1 subgroups. This is important given that previous results have not identified a one-to-one spatial correspondence between the pairwise anatomical distances and pairwise spatial firing correlations between neurons.[45]

We first examined the anatomical distribution of place cells. As shown in Figure S4B, place cells are defined according to the distribution in their spatially binned firing rates and the similarities in rates of neighboring spatial bins. Place cells are observed among all detected anatomical clusters. Importantly, place cells of the same cluster can either be neighboring each other or have large distances between them. The pairwise distance between intra-cluster place cells, as well as all intra-cluster neurons, is lower than that with all place cell pairs (i.e., independent of their clustering), but there was no significant difference noted between intra-cluster place cells and all intra-cluster cells (Figure S4C). Thus, neurons with strong location-specific activity are just a sub-population of the defined clusters whose activation patterns occur across the same second-long period of time. The pairwise temporal correlation of intra-cluster place cells, and all intra-cluster neurons, are higher than that of all place cell pairs (Figure S4D). Thus, the grouping of neurons by temporal correlation captures neurons that are active over the same second-long period of time, irrespective of whether their activity can be strongly place-specific.

We next examined the relationship of temporally correlated activity to the distribution of location-specific activity for neurons of the same and different clusters. We measured spatially defined activity maps of CA1 neurons by calculating their firing rates within 1 cm*1 cm spatial bins. We also calculated the averaged spatial activity maps across individual neurons of the same cluster to construct the "ensemble activity map" for that cluster. Interestingly, we find that many temporally correlated CA1 neurons tend to share environmental location-specific tuning, and their ensemble activity clearly maximize across a specific sub-region of environmental space (Figure 2). To quantify the extent of the coverage difference between different neuron clusters, we calculated the pairwise overlap level between ensemble activity maps from all clusters of each individual mice. We define the "major field" as the center portion of ensemble activity maps

that have higher than 50% of the maximum activity level across the activity map (Figure S7A), and pairwise overlap level is calculated as the ratio between overlapped area and total area of the two major fields. When we pooled the overlap levels from all mice together, we noted low level of overlapping between major fields of a large fraction of ensemble activity map pairs, with 93.21% of pairs having lower than 25% of their major fields overlapping with each other (Figure S7C). Similar results were also noted when we only include the place cells in each cluster (Figures S12 and S13).

In the meantime, while many individual intra-cluster neurons have maximal activity within the sub-region covered by cluster ensemble activity map, some neurons within the same temporally defined cluster can have spatially distinct activity distributions, that the firing peaks for individual neurons of a cluster can be distributed across the full space of the environment (Figures 2B, 2E, and 2H black dots). We think this is consistent with a model in which much of the temporal correlation in activity occurs as a combined consequence of the locations of spatially specific activity for neurons, and the distances as well as trajectories taken by animals across second-long period of time. In this way, many neurons of a cluster will have place fields partially constrained to a sub-region of the arena given that animals may remain in the same area over many second-long period. Meanwhile, considering Figure S4, place cells only constitute part of the intra-cluster neuron populations. Hence, neurons showing activity outside the high ensemble activity region may be fulfilling their functions differently from place encoding, while they also co-activate with other intra-cluster neurons to support the cognitive process inside the high ensemble activity region.

To further investigate the interaction between spatial and temporal components of activity correlation within clusters, we also examined the relationships between pairwise temporal correlation and pairwise activity map correlations. Temporal activity correlations are overall positively correlated with spatial map correlations between neuron pairs sharing the same anatomical cluster (Figures 2C, 2F, and 2I also Figure S5). Meanwhile, at different temporal correlation levels, the spatial map correlation variates, which follows our observation that intra-cluster neurons can display their primary firing fields at different locations across the arena. These results further support our observation that intra-cluster CA1 principal neuron pairs displaying relatively higher temporal correlation also display more similar spatial tunings. Moreover, these results highlight that the anatomical clustering of CA1 neurons discovered herein reflect temporally correlated activation of neuron sub-groups over second-long period, as opposed to an anatomical clustering organized strictly and exclusively by the location-specific firing of neurons.

Anatomical clustering of co-active neuron populations is dynamic

As anatomical clusters exhibit sensitivity to the specific environmental locations visited across time, we asked if different environments would yield different patterns of clustering. To test this, we compared anatomical clustering for temporally derived neuron sub-groups when animals explored circle-, triangle-, or square-shaped environments (Figure 3A, each environment also bore unique visual cues along their walls). Anatomical clustering based on groupings of temporally correlated neurons was observed for all three environments (Figure 3B). The average spatial activity map correlations between the first and second half of the same sessions, and between sessions recorded in the same environment on different days, did not differ significantly (Figure 3C). However, anatomical clustering appears to vary across days and across environments. We measured the level of cluster overlap both for different environments and for the same environment on different days. The level of cluster overlap is significantly higher than the chance level for all conditions tested (Figure 3D). This shows that CA1 neurons in each anatomical cluster exhibit a degree of stability in their being active across the same second-long period of environmental exploration, which is true for different environments and for the same environment on different days. Though the mean overlap between neurons forming each group tends to be higher for the same environment as compared to different environments, it is not significant (Figure 3D). We note that cluster overlap across different environments does not imply that the distribution of location-specific firing across neurons is the same for different environments.

We then considered the possibility that an environment yielding more stable and similar trajectories through space might yield more robust stability in anatomical clustering. To test this, we compared anatomical cluster membership and spatial activity patterns when animals traveled along a horizontally or vertically oriented linear track (Figure 3E, both track orientations gave a view to the same set of global visual cues in the recording room). As the track defines a space that can be moved or reoriented within a larger, directly visible allocentric space (defined by the recording room walls), activity maps for different

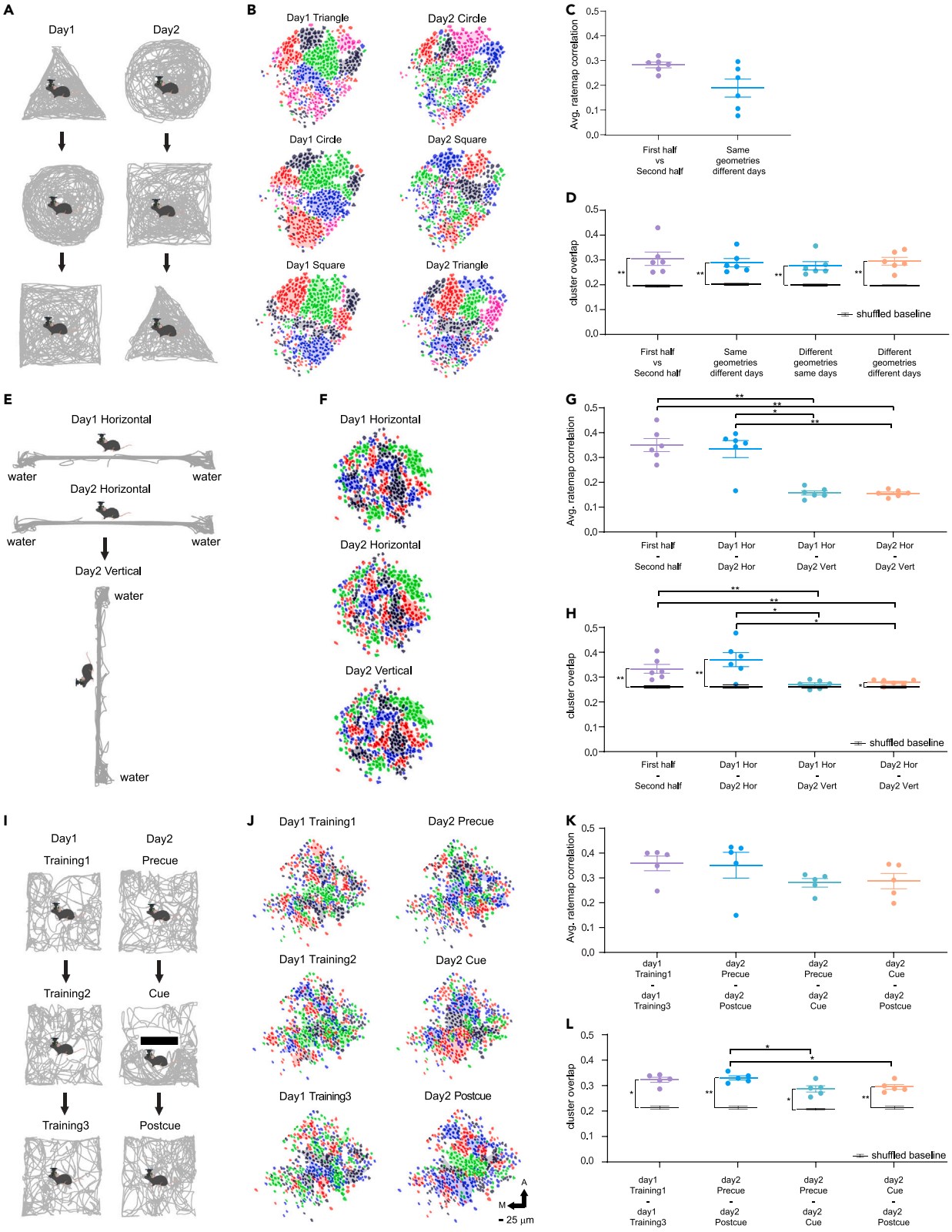
A
Day1
Day2
B
Day1 Triangle
Day2 Circle
Day1 Circle
Day2 Square
Day1 Square
Day2 Triangle
C
Avg. ratemap correlation
First half vs Second half
Same geometries different days
D
cluster overlap
shuffled baseline
First half vs Second half
Same geometries different days
Different geometries same days
Different geometries different days
E
Day1 Horizontal
water
Day2 Horizontal
Day2 Vertical
F
Day1 Horizontal
Day2 Horizontal
Day2 Vertical
G
Avg. ratemap correlation
First half - Second half
Day1 Hor - Day2 Hor
Day1 Hor - Day2 Vert
Day2 Hor - Day2 Vert
H
cluster overlap
shuffled baseline
I
Day1
Day2
Training1
Precue
Training2
Cue
Training3
Postcue
J
Day1 Training1
Day2 Precue
Day1 Training2
Day2 Cue
Day1 Training3
Day2 Postcue
A
M
25 µm
K
Avg. ratemap correlation
day1 Training1 - day1 Training3
day2 Precue - day2 Postcue
day2 Precue - day2 Cue
day2 Cue - day2 Postcue
L
cluster overlap
shuffled baseline

Figure 3. Anatomical cluster-specific calcium event activities vary across different environments

(A) Experiment schematic. Six mice explored inside three different types of arenas (triangle, circle, and square), each arena for 12 min. The order of exploration in the first and second day is illustrated in the schematic.

(B) Anatomical clusters in hippocampal CA1 in one representative mouse for each of these trials. The scale bars for B, F, J are the same as displayed in J

(C) Average activity map correlation between the two-halves of each trial and trials with the same geometry on different days. No significant difference is found between the two conditions (first half - second half: 0.2825 ± 0.0113, same geometry different days: 0.1889 ± 0.0363, p = 0.0931, two-tailed Wilcoxon rank-sum test, Data are presented as the mean ± SEM, N = 6 mice).

(D) Cluster overlap between the first and second halves of each trial, between the same geometry trials on different days, between different geometry trials on the same day, and between different trials on different days. No significant difference is found between these conditions (first half - second half: 0.2950 ± 0.0155, same geometry different days: 0.3051 ± 0.0268, different geometry same days: 0.2889 ± 0.0168, different geometry different days: 0.2764 ± 0.0168. first half - second half vs. same geometry different days: p > 0.9999; first half - second half vs. different geometry same days: p > 0.9999; first half - second half vs. different geometry different days: p = 0.3939; same geometry different days vs. different geometry same days: p = 0.8182; same geometry different days vs. different geometry different days: p = 0.4848; different geometry same days vs. different geometry different days: p = 0.4848; two-tailed Wilcoxon rank-sum test, Data are presented as the mean ± SEM, N = 6 mice), while all the cluster overlap distributions are significantly higher than their corresponding shuffled baseline (first half - second half baseline: 0.2117 ± 0.0014, same geometry different days baseline: 0.2125 ± 0.0031, different geometry same days baseline: 0.2166 ± 0.0032, different geometry different days baseline: 0.2124 ± 0.0031, first half - second half vs. its baseline: p = 0.0022, same geometry different days vs. its baseline: p = 0.0022, different geometry same days vs. its baseline: p = 0.0022, different geometry different days vs. its baseline: p = 0.0022, two-tailed Wilcoxon rank-sum test, Data are presented as the mean ± SEM, N = 6 mice).

(E) Experiment schematic. Six mice conducted exploration on a horizontal linear track on the first day. On the second day, they first repeated the exploration on the track with previous day's settings. After that, the track was rotated 90° clockwise, and the mice conducted another exploration on the rotated track.

(F) Anatomical cluster organization for one representative mouse for each of these three conditions.

(G) Average activity map correlation between the first and second halves of the same trials, and between the two horizontal track trials. (First and second halves: 0.3503 ± 0.0261, day 1 horizontal to day 2 horizontal: 0.3343 ± 0.0344, day 1 horizontal to day 2 vertical: 0.1573 ± 0.0085, day 2 horizontal to day 2 vertical: 0.1558 ± 0.0057. first and second half vs. day 1 horizontal to day 2 horizontal: p = 0.8182, first and second half vs. day 1 horizontal to day 2 vertical: p = 0.0022, first and second half vs. day 2 horizontal to day 2 vertical: p = 0.0022, day 1 horizontal to day 2 horizontal vs. day 1 horizontal to day 2 vertical: p = 0.0087, day 1 horizontal to day 2 horizontal vs. day 2 horizontal to day 2 vertical: p = 0.0043, day 1 horizontal to day 2 vertical vs. day 2 horizontal to day 2 vertical: p = 0.9372. two-tailed Wilcoxon rank-sum test, Data are presented as the mean ± SEM, N = 6 mice).

(H) Cluster overlap between the first and second halves of the same trials, between day 1 horizontal to day 2 horizontal, between day 1 horizontal to day 2 vertical, and between day 2 horizontal to day 2 vertical, (First and second halves: 0.3333 ± 0.0177, day 1 horizontal to day 2 horizontal: 0.3702 ± 0.0283, day 1 horizontal to day 2 vertical: 0.2706 ± 0.0283, day 2 horizontal to day 2 vertical: 0.2782 ± 0.0048. first and second half vs. day 1 horizontal to day 2 horizontal: p = 0.3939, first and second half vs. day 1 horizontal to day 2 vertical: p = 0.0043, first and second half vs. day 2 horizontal to day 2 vertical: p = 0.0022, day 1 horizontal to day 2 horizontal vs. day 1 horizontal to day 2 vertical: p = 0.0260, day 1 horizontal to day 2 horizontal vs. day 2 horizontal to day 2 vertical: p = 0.0260, day 1 horizontal to day 2 vertical vs. day 2 horizontal to day 2 vertical: p = 0.4848. two-tailed Wilcoxon rank-sum test, Data are presented as the mean ± SEM, N = 6 mice). Except day 1 horizontal – day 2 vertical combination, all other cluster overlap distributions are significantly higher than their corresponding shuffled baseline (First and second halves baseline: 0.2616 ± 0.0047, day 1 horizontal to day 2 horizontal baseline: 0.2634 ± 0.0066, day 1 horizontal to day 2 vertical baseline: 0.2606 ± 0.0036, day 2 horizontal to day 2 vertical baseline: 0.2606 ± 0.0036. First and second halves vs. its baseline: p = 0.0026, day 1 horizontal to day 2 horizontal baseline vs. its baseline: p = 0.0043, day 1 horizontal to day 2 vertical vs. its baseline: p = 0.4848, day 2 horizontal to day 2 vertical vs. its baseline: p = 0.0260, two-tailed Wilcoxon rank-sum test, Data are presented as the mean ± SEM, N = 6 mice).

(I) Experiment schematic. Five mice conducted 10-min exploration in the same square box for three times on the first day. On the second day, a barrier was placed in the middle of the box in the second trial.

(J) Anatomical clusters for one representative mouse for the trials described in I.

(K) Average activity map correlation for the trial combinations (training1 and training3: 0.3586 ± 0.0294, pre-cue and post-cue: 0.3512 ± 0.0517, pre-cue and cue: 0.2805 ± 0.0173, post-cue and cue: 0.2872 ± 0.0309. training1 and training3 vs. pre-cue and post-cue: p = 0.4206, training1 and training3 vs. pre-cue and cue: p = 0.0952, training1 and training3 vs. post-cue and cue: p = 0.1508, pre-cue and post-cue vs. pre-cue and cue: p = 0.1508, pre-cue and post-cue vs. post-cue and cue: p = 0.1508, pre-cue and cue vs. post-cue and cue: p > 0.9999, two-tailed Wilcoxon rank-sum test, Data are presented as the mean ± SEM, N = 6 mice).

(L) Cluster similarities between the training1 and training3 trial in the first day, and between the pre-cue and post-cue, pre-cue and cue, post-cue, and cue trials in the second day (training1 and training3: 0.3229 ± 0.0099, pre-cue and post-cue: 0.3304 ± 0.0083, pre-cue and cue: 0.2872 ± 0.0123, post-cue and cue: 0.2950 ± 0.0094. training1 and training3 vs. pre-cue and post-cue: p = 0.8413, training1 and training3 vs. pre-cue and cue: p = 0.1508, training1 and training3 vs. post-cue and cue: p = 0.1508, pre-cue and post-cue vs. pre-cue and cue: p = 0.0317, pre-cue and post-cue vs. post-cue and cue: p = 0.0317, pre-cue and cue vs. post-cue and cue: p = 0.6905, two-tailed Wilcoxon rank-sum test, Data are presented as the mean ± SEM, N = 6 mice). All the cluster overlap distributions are significantly higher than their corresponding shuffled baseline (training1 and training3 baseline: 0.2655 ± 0.0075, pre-cue and post-cue: 0.2607 ± 0.0033, pre-cue and cue: 0.3229 ± 0.0099, post-cue and cue: 0.3304 ± 0.0083. training1 and training3 vs. its baseline: p = 0.0159, pre-cue and post-cue vs. its baseline: p = 0.0079, pre-cue and cue vs. its baseline: p = 0.0159, post-cue and cue vs. its baseline: p = 0.0079, two-tailed Wilcoxon rank-sum test, Data are presented as the mean ± SEM, N = 6 mice). Asterisks are defined as p ≤ 0.05 *, p < 0.01 **, p < 0.001,***.

configurations of the track relative to the room could be compared for similarity; this was not possible for the open-field arena exploration experiments where an obvious means to align environments is not given. By rotating the track, the global environment perceived by animals for the same locations on the track will be differentiated. The clusters based on groupings of temporally correlated neurons recorded from animals on linear tracks are robust (Figure 3F). We first calculate the spatial activity map correlations between the first and second halves of individual recording sessions, and between two different sessions using the

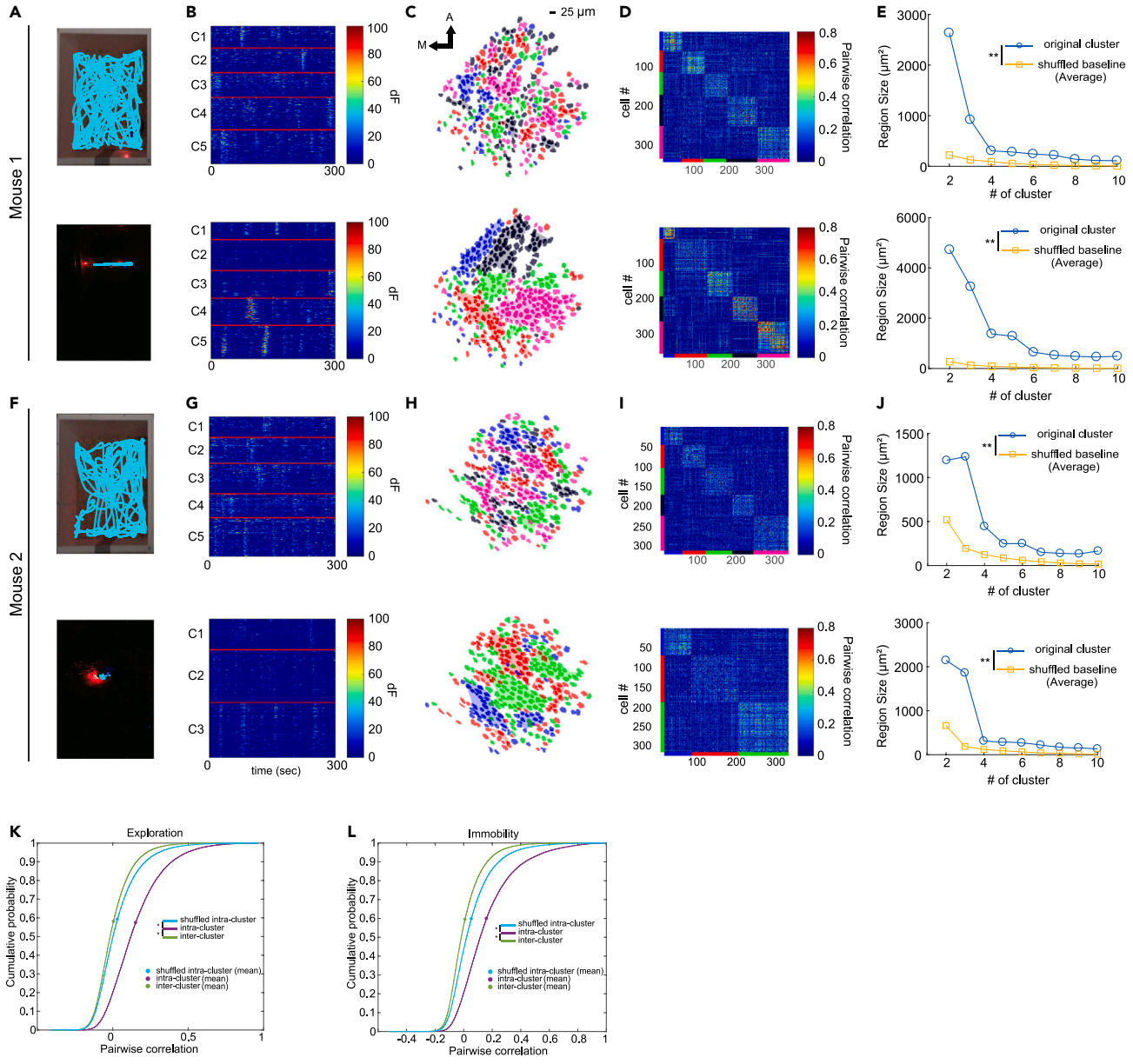

Figure 4. Comparisons of anatomical clusters during active exploration and long-term immobility

(A and F; upper portion of each panel) Two example mice actively explored in an open arena (blue traces, square box) (A, F; lower portion of panel) The example mice were immobile in their home cage (square box) which was dimly lit.

(B and G; upper portion of panel) Raw calcium activity traces of individual neurons of the mice during active exploration of the arena. (B, G; lower portion of panel) Raw calcium activity trace of individual neurons of the same mice grouped by anatomical clustering during long periods of immobility.

(C, H; upper portion of panel) Anatomical clusters during active exploration of the arena by the example mice. (C and H; lower portion of panel) Anatomical clusters during long periods of immobility.

(D and I; upper portion of panel) Pairwise correlation matrix of neurons during exploration of the example mice. (D, I; lower portion of panel) Pairwise correlation matrix of neurons during immobility of the example mice.

(E and J; upper portion of panel) Anatomical cluster patch size for different number of clusters during exploration. (E, J; lower portion of panel) Anatomical cluster patch size for different number of clusters during immobility. Blue circle: Patch size of the original anatomical clusters. Yellow square: average size of the distribution of shuffled cluster patches. Overall, original clusters' patch size across different choices of cluster numbers are significantly higher than that of shuffled baseline for both exploration and immobility across different cluster numbers (E upper panel: $p = 0.0039$; E lower panel: $p = 0.0039$; J upper panel: $p = 0.0039$; J lower panel: $p = 0.0039$. Wilcoxon matched pair signed rank test, $N = 9$ cluster numbers).

(K and L) Cumulative probability distributions of intra- and inter-cluster pairwise temporal correlations of individual neuron pairs during active exploration (K) or immobile periods (L) for all mice tested. Shuffled intra-cluster pairwise cross-correlation is included as well in both K and L. (K) During exploration

Figure 4. *Continued*
intra-cluster correlation is significantly higher than both shuffled and inter-cluster correlation (intra-cluster: 0.1422 ± 0.0010; inter-cluster: 0.0032 ± 0.0002; shuffled intra-cluster: 0.0314 ± 2.4697*10^{-5}. intra-cluster versus inter-cluster: p = 1.9134*10^{-29}, intra-cluster versus shuffled: p = 8.4786*10^{-24}, two-sample Kolmogorov-Smirnov test, Data are presented as the mean ± SEM). (L) During immobility the intra-cluster correlation is significantly higher than both shuffled and inter-cluster correlation (intra-cluster: 0.1448 ± 0.0001; inter-cluster: 0.0081 ± 0.0003; shuffled: 0.0491 ± 2.2288*10^{-5}. intra-cluster versus inter-cluster: p = 5.2291*10^{-22}, intra-cluster versus shuffled: p = 1.5743*10^{-12}, two-sample Kolmogorov-Smirnov test, Data are presented as the mean ± SEM, N = 6 mice). Asterisks are defined as p ≤ 0.05 *, p < 0.01 **, p < 0.001,***.

same horizontal orientation. The correlation levels between the halves and same direction trials are in the same level with the lap-by-lap rate map correlation within each trial (Figure S15) but are significantly higher than those for the horizontally versus vertically oriented track (Figure 3G), indicating a strong influence of location and orientation on spatial firing patterns as expected. The level of cluster overlaps for the first and second halves of each track orientation and across days using the same orientation is beyond that expected by chance (Figure 3G; comparisons within columns). Next, we asked if there is greater anatomical cluster overlap for the same versus different track orientations. Anatomical clusters have a significantly greater overlap for the same orientation in accordance with the greater degree of pairwise activity map correlations (horizontal or vertical orientation, Figure 3H; comparisons across columns). We attribute the higher clustering overlap for the two horizontal orientation track runs as likely reflecting the constraint on the animal to only two trajectories through the observable environment; this constraint does not characterize the free exploration of the circle, triangle, or square-shaped arenas on different days or across different time periods of the same session.

To further examine how clustering stability may reflect the difference in exploration behavior induced by environment change, we utilized a task in which a barrier is introduced in the center of the square arena, which can alter the exploration trajectory of the animals compared with that of empty arena (Figures 3I and 3J). Although no significant difference was noted in terms of activity map correlation (Figure 3K), we again noted a significant reduction in cluster overlap between the empty box trials and the barrier trials, while between two open box trials, even on different days, the anatomical cluster overlap shows no significant differences (Figure 3L). Altogether, the above results indicate that anatomical clusters display much stability yet are versatile and dynamic in their organization during active behavioral exploration of different environments.

Anatomical clusters and behavioral states

Having characterized the dynamics and stability of CA1 anatomical clusters of co-active neurons, we next asked if they persist across distinct behavioral states. We compared the behavioral states of active exploration versus immobility within the same environment (Figures 4A, 4B, 4F, and 4G). To facilitate immobility, we imaged CA1 neurons while animals were in their home cage inside a dark box under dim lighting. Visual inspection of the layout of temporally correlated neuron groups during immobile periods revealed that anatomical clusters are as robust as those during behavioral exploration (Figures 4C, 4D, 4E, 4H, 4I, and 4J). These results indicate that anatomical clusters are present even during immobility.

To determine the significance of anatomical clustering across the behavioral states of active exploration versus immobility, we compared the cumulative probability distribution of intra-cluster and inter-cluster temporal correlations for neuron pairs under active exploration and immobility states. During the exploration period, intra-cluster neuron pair correlations are significantly higher than both shuffled baseline and inter-cluster correlations (Figure 4K). Similarly, during immobility, intra-cluster neuron pair correlations are significantly higher than both shuffled baseline and inter-cluster correlations (Figure 4L). These results suggest that while the temporal correlations in activity seen for anatomical clusters of CA1 neurons are related to the actual exploration pattern for an environment (Figure 2), temporal clustering is also subject to the influence of internal dynamics and connectivity. In this way, clustering of activity and anatomical proximity among neuron sub-groups may form CA1 hippocampal activity sequences for encoding and memory of locomotor and non-locomotor episodes.

DISCUSSION

Neighboring neurons with similar response properties form topographic modular structures in sensory areas of the neocortex.[47,48] To date, most approaches to detecting such one-to-one correspondences between the sites of location-specific firing for individual neurons and their locations with the space of CA1

have not found evidence for a strict, metric form of topographic representation of environmental location.[45] Instead, hippocampal neurons underlying spatial navigation and memory formation are thought to have a non-topographical, distributed organization. Yet, work addressing this question has focused on the response properties of very closely neighboring neurons recorded on the same electrode in comparison to neurons recorded on different electrodes at larger distances from each other. Furthermore, these experiments have generated contradictory results.[32,45,49] Neurons with the same place field tuning can be located anywhere in CA1,[23] yet under more complicated tasks such as associating positions with rewards, it has been reported that neurons with the same tuning tend to neighbor one another.[18] Similar anatomically organized CA1 principal neuron sub-populations are also identified after association learning.[34] These results suggest that the anatomical organization of the hippocampus is not yet fully understood and that there may be yet undiscovered principles of connectivity that guide the expression of activity sequences.

Our results show that a very different form of topographical organization not examined in prior work is found when CA1 pyramidal neurons are clustered according to which neurons are activated over second-long time periods. Here, clustering, in the form of cluster members being activated within the same second-long time periods, is accompanied by clustering of members within contiguous areas or "patches" of the CA1 region being imaged. Notably, this form does not imply that neurons of the same cluster will necessarily exhibit location-specific firing over overlapping locations in the environment. Further, this form does not imply that members of a cluster are adjacent, but, rather, that they lie over a potentially broader spatial range within a contiguous region of CA1; cluster members may be neighboring cells or lie hundreds of microns apart. The CA1 topographical organization of anatomical clusters follows the seconds-scale temporal correlation among large groups of neurons spread over relatively broad regions of anatomical space. Our approach stands in contrast to the approach used in earlier work in which smaller hippocampal neuron groups of closely neighboring versus non-neighboring neurons were identified according to whether they had been recorded on the same or a different recording tetrode.[45] Correlations in the spatial activity maps for same-tetrode versus different-tetrode neuron groups were used to assess the presence or absence of topographic organization. In the present study, we find that neurons with non-overlapping location-specific firing fields can be also assigned to the same cluster, in addition, neurons sharing the same cluster identity can be so anatomically distant from each other that recording them on the same tetrode would be extremely unlikely. For these reasons, we suggest that the replication of our findings using electrophysiology in rats or in mice would demand the utilization of a tightly spaced (across anterior-posterior and medial-lateral dimensions) and dense array of recording electrodes. Compared to conventional electrophysiological approaches, optical imaging of cell activity allows for continuous sampling across larger sub-spaces of the CA1 region to better address the issue of topography and to search for any of multiple forms of it. In the present work, the quantification of temporal correlations between CA1 neurons imaged over a broad view field for several seconds serendipitously yielded discovery of near-neighbor anatomical clustering in the hippocampal CA1 region.

Anatomical clusters in hippocampal sub-region CA1 have several notable anatomical and functional characteristics. First, they are defined in the present work by temporal correlations between CA1 neurons on the order of seconds. Many, but not all, of the recorded neurons exhibit place-specific activity by conservative criteria. By focusing on temporal correlations in firing patterns, our approach examines the dynamics of hippocampal ensembles without employing filters according to a simplified model wherein CA1 excitatory neurons exhibit only single place fields with highly reliable visit-to-visit activation and robustness to trajectory taken through a location. Thus, at least for active foraging behaviors, the temporal correlations in activity reflect in part the sequencing of spatially tuned ensemble activity patterns that accompany specific trajectories through an environment. Our approach may also be better able to detect co-activation patterns under circumstances where the recording technique (imaging versus electrophysiological) and/or the species (e.g., rat versus mouse) may be associated with differences in the degree and reliability of spatial tuning. With respect to spatially versus temporally correlated activity, it is also relevant that we observed anatomical clustering for both active exploration and immobile behavioral states. The latter, of course, precludes a spatial approach to defining correlated activity. This suggests that more internally driven dynamics are organized, at least in part, according to the layout of neurons across the space of CA1. A second functional characteristic is that anatomical clusters do not always constitute a single continuous region; a single anatomical cluster may include a non-contiguous island of neurons that is relatively remote from the main cluster. Finally, when we measured anatomical cluster overlap as animals explored

different environments, we found that they are dynamic in their organization. In other words, the anatomical distribution of clusters has a "mix-and-match" quality wherein the observed topography is specific to the environment. Temporally correlated clusters of neurons and the sub-regions they occupy in CA1 can be organized in a combinatorial fashion that matches the diversity of experience across environments.

The question as to what circuitry leads to temporal activity correlations for anatomically clustered neurons is complex. Multiple non-random distributions of connectivity co-exist in CA1 including inputs from entorhinal cortex, subiculum, and CA3, all of which vary systematically along the transverse and septo-temporal axes of hippocampus.[50] Yet, anatomical clustering observed in the present work is dynamic and does not neatly follow obvious medial/lateral or anterior/posterior patterns. Another possible source of anatomical organization are patterns of hippocampal GABAergic interneuronal axonal arbors. CA1 interneurons are heterogeneous in their dendritic and axonal arbors and are tightly integrated into the temporal and spatial tuning dynamics of CA1 pyramidal cells.[25,27,51,52] Through broad-scale changes in firing rates, sub-populations of interneurons appear to influence CA1 pyramidal neuron spatial tuning over the space of experimental arenas such as those used in the present work.[11,53] Thus, we speculate that the dynamic and fractured topography of CA1 neuron activation patterns observed in the present study are the product of time-based and environment-based dynamic reorganization of activity patterns among CA1 interneurons and the organization of excitatory inputs according to the transverse and longitudinal axes.

Geiller et al.'s recent study provided a model hypothesizing CA1 pyramidal cells are embedded inside a subnetwork including neighboring pyramidal cells and interneurons. In our results, the anatomical distribution of neighboring intra-cluster neurons to place cells, and the distance-temporal correlation relationship of temporally clustered pyramidal neurons is comparable to what Geiller et al. study presented. Our observation is based on different analytical approaches, which make us believe that we are measuring the physiological properties of CA1 pyramidal neuron populations rather than coincidence caused by non-neuron structures or specific experimental settings. Meanwhile, the idea of recurrently connected neighboring pyramidal cells could be another potential source of the CA1 pyramidal cell organization we are seeing here and is worth further study.

Overall, our findings imply that episodic memories for random trajectories through an environment may be contained within sub-spaces of CA1 and that the activation of CA1 sub-regions could trigger recall of the environmental locations already visited within a single exploration session. This is consistent with recent work demonstrating that the co-activation of neurons over timescales of several seconds can drive the changes in synaptic efficacy that are thought to define memories.[19] Alternatively, activation of clusters could be involved in the control of behavioral output itself through CA1 outputs to prefrontal cortex[54] or retrosplenial cortex.[55] Also, anatomical clusters may guide neural activity that contributes to spatial navigation and episodic memory.

Limitation of the study

Although we have performed a number of analyses to make sure our imaging data only contains the response of principal cells, we acknowledge that one-photon imaging has intrinsic limitations in distinguishing multi-plane and background signals. Further studies can utilize 2-photon imaging or electrophysiology technics with high anatomical resolution to further investigate the topic. Also, detailed investigations should be performed to examine the observations described here in environments with different sizes, in different types of tasks, and animal species. While CNMF-E is widely used in neuron extraction from 1-photon calcium imaging recordings, deep-learning-based neuron identification tools such as DeepWonder have been noted for better modeling of the background in fluorescence imaging.[56] Future research may acquire neuron extraction results from recently developed tools.

STAR★METHODS

Detailed methods are provided in the online version of this paper and include the following:

- KEY RESOURCES TABLE
- RESOURCE AVAILABILITY
  - Lead contact
  - Material availability
  - Data and code availability

SUPPLEMENTAL INFORMATION

Supplemental information can be found online at https://doi.org/10.1016/j.isci.2023.106703.

ACKNOWLEDGMENTS

This work was supported by US National Institutes of Health (NIH) grants R01 NS104897 and RF1 AG065675. Todd C. Holmes is supported by R35 GM127102. We thank Dr. Suoqin Jin for his advice on our clustering algorithm, and Dr. Pengcheng Zhou for his advice on handling potential dendritic components in CNMF-E's extraction results.

AUTHOR CONTRIBUTIONS

X.L. and Q.Y. performed viral injection, imaging, and behavioral experiments. L.C performed calcium imaging and behavior data analysis. L.C., X.L., S.F.G., T.C.H., D.A.N., and X.X. analyzed the data, prepared the figures, and wrote the article. X.X. designed and oversaw the project.

DECLARATION OF INTERESTS

All authors disclose no conflict of interests for this work.

Received: November 24, 2021
Revised: September 27, 2022
Accepted: April 15, 2023
Published: April 21, 2023

REFERENCES

1. O'Keefe, J., and Dostrovsky, J. (1971). The hippocampus as a spatial map. Preliminary evidence from unit activity in the freely-moving rat. Brain Res. *34*, 171–175. https://doi.org/10.1016/0006-8993(71)90358-1.

2. O'Keefe, J., and Burgess, N. (1996). Geometric determinants of the place fields of hippocampal neurons. Nature *381*, 425–428. https://doi.org/10.1038/381425a0.

3. Krupic, J., Bauza, M., Burton, S., and O'Keefe, J. (2018). Local transformations of the hippocampal cognitive map. Science *359*, 1143–1146. https://doi.org/10.1126/science.aao4960.

4. Skaggs, W.E., and McNaughton, B.L. (1996). Replay of neuronal firing sequences in rat Hippocampus during sleep following spatial experience. Science *271*, 1870–1873. https://doi.org/10.1126/science.271.5257.1870.

5. Pfeiffer, B.E., and Foster, D.J. (2013). Hippocampal place-cell sequences depict

future paths to remembered goals. Nature *497*, 74–79. https://doi.org/10.1038/nature12112.

6. McNaughton, B.L., Barnes, C.A., and O'Keefe, J. (1983). The contributions of position, direction, and velocity to single unit activity in the hippocampus of freely-moving rats. Exp. Brain Res. *52*, 41–49. https://doi.org/10.1007/BF00237147.

7. O'Neill, J., Senior, T., and Csicsvari, J. (2006). Place-selective firing of CA1 pyramidal cells during sharp wave/ripple network patterns in exploratory behavior. Neuron *49*, 143–155. https://doi.org/10.1016/j.neuron.2005.10.037.

8. O'Keefe, J., and Recce, M.L. (1993). Phase relationship between hippocampal place units and the EEG theta rhythm. Hippocampus *3*, 317–330. https://doi.org/10.1002/hipo.450030307.

9. Markus, E.J., Barnes, C.A., McNaughton, B.L., Gladden, V.L., and Skaggs, W.E. (1994). Spatial information content and reliability of hippocampal CA1 neurons: effects of visual input. Hippocampus *4*, 410–421. https://doi.org/10.1002/hipo.450040404.

10. Wood, E.R., Dudchenko, P.A., Robitsek, R.J., and Eichenbaum, H. (2000). Hippocampal neurons encode information about different types of memory episodes occurring in the same location. Neuron *27*, 623–633. https://doi.org/10.1016/S0896-6273(00)00071-4.

11. Wilson, M.A., and McNaughton, B.L. (1993). Dynamics of the hippocampal ensemble code for space. Science *261*, 1055–1058. https://doi.org/10.1126/science.8351520.

12. Ferbinteanu, J., and Shapiro, M.L. (2003). Prospective and retrospective memory coding in the Hippocampus. Neuron *40*, 1227–1239. https://doi.org/10.1016/S0896-6273(03)00752-9.

13. Ainge, J.A., van der Meer, M.A.A., Langston, R.F., and Wood, E.R. (2007). Exploring the role of context-dependent hippocampal activity in spatial alternation behavior. Hippocampus *17*, 988–1002. https://doi.org/10.1002/hipo.20301.

14. Nitz, D.A. (2006). Tracking route progression in the posterior parietal cortex. Neuron *49*, 747–756. https://doi.org/10.1016/j.neuron.2006.01.037.

15. Pastalkova, E., Itskov, V., Amarasingham, A., and Buzsáki, G. (2008). Internally generated cell assembly sequences in the rat Hippocampus. Science *321*, 1322–1327. https://doi.org/10.1126/science.1159775.

16. Karlsson, M.P., and Frank, L.M. (2009). Awake replay of remote experiences in the hippocampus. Nat. Neurosci. *12*, 913–918. https://doi.org/10.1038/nn.2344.

17. Brown, E.N., Frank, L.M., Tang, D., Quirk, M.C., and Wilson, M.A. (1998). A statistical paradigm for neural spike train decoding applied to position prediction from ensemble firing patterns of rat hippocampal place cells. J. Neurosci. *18*, 7411–7425. https://doi.org/10.1523/JNEUROSCI.18-18-07411.1998.

18. Grieves, R.M., Wood, E.R., and Dudchenko, P.A. (2016). Place cells on a maze encode routes rather than destinations. Elife *5*, e15986. https://doi.org/10.7554/eLife.15986.

19. Bittner, K.C., Milstein, A.D., Grienberger, C., Romani, S., and Magee, J.C. (2017). Behavioral time scale synaptic plasticity underlies CA1 place fields. Science *357*, 1033–1036. https://doi.org/10.1126/science.aan3846.

20. Marr, D., and Brindley, G.S. (1971). Simple memory: a theory for archicortex. Philos. Trans. R. Soc. Lond. B Biol. Sci. *262*, 23–81. https://doi.org/10.1098/rstb.1971.0078.

21. Guzman, S.J., Schlögl, A., Frotscher, M., and Jonas, P. (2016). Synaptic mechanisms of pattern completion in the hippocampal CA3 network. Science *353*, 1117–1123. https://doi.org/10.1126/science.aaf1836.

22. Harris, K.D., Henze, D.A., Hirase, H., Leinekugel, X., Dragoi, G., Czurkó, A., and Buzsáki, G. (2002). Spike train dynamics predicts theta-related phase precession in hippocampal pyramidal cells. Nature *417*, 738–741. https://doi.org/10.1038/nature00808.

23. McNaughton, B., and Morris, R. (1987). Hippocampal synaptic enhancement and information storage within a distributed memory system. Trends Neurosci. *10*, 408–415.

24. Treves, A., and Rolls, E.T. (1994). Computational analysis of the role of the hippocampus in memory. Hippocampus *4*, 374–391. https://doi.org/10.1002/hipo.450040319.

25. Klausberger, T. (2009). GABAergic interneurons targeting dendrites of pyramidal cells in the CA1 area of the hippocampus. Eur. J. Neurosci. *30*, 947–957. https://doi.org/10.1111/j.1460-9568.2009.06913.x.

26. Freund, T.F., and Buzsáki, G. (1996). Interneurons of the hippocampus. Hippocampus *6*, 347–470. https://doi.org/10.1002/(SICI)1098-1063(1996)6:4<347::AID-HIPO1>3.0.CO;2-I.

27. Klausberger, T., Marton, L.F., O'Neill, J., Huck, J.H.J., Dalezios, Y., Fuentealba, P., Suen, W.Y., Papp, E., Kaneko, T., Watanabe, M., et al. (2005). Complementary roles of cholecystokinin- and parvalbumin-expressing GABAergic neurons in hippocampal network oscillations. J. Neurosci. *25*, 9782–9793. https://doi.org/10.1523/JNEUROSCI.3269-05.2005.

28. Giocomo, L.M. (2016). Environmental boundaries as a mechanism for correcting and anchoring spatial maps. J. Physiol. *594*, 6501–6511. https://doi.org/10.1113/JP270624.

29. Gothard, K.M., Skaggs, W.E., and McNaughton, B.L. (1996). Dynamics of mismatch correction in the hippocampal ensemble code for space: interaction between path integration and environmental cues. J. Neurosci. *16*, 8027–8040. https://doi.org/10.1523/JNEUROSCI.16-24-08027.1996.

30. Knierim, J.J., Kudrimoti, H.S., and McNaughton, B.L. (1995). Place cells, head direction cells, and the learning of landmark stability. J. Neurosci. *15*, 1648–1659. https://doi.org/10.1523/JNEUROSCI.15-03-01648.

31. Ito, H.T., Moser, E.I., and Moser, M.-B. (2018). Supramammillary nucleus modulates spike-time coordination in the prefrontal-thalamo-hippocampal circuit during navigation. Neuron *99*, 576–587.e5. https://doi.org/10.1016/j.neuron.2018.07.021.

32. Muller, R.U., and Kubie, J.L. (1987). The effects of changes in the environment on the spatial firing of hippocampal complex-spike cells. J. Neurosci. *7*, 1951–1968. https://doi.org/10.1523/JNEUROSCI.07-07-01951.

33. Wilson, M.A., and McNaughton, B.L. (1994). Reactivation of hippocampal ensemble memories during sleep. Science *265*, 676–679. https://doi.org/10.1126/science.8036517.

34. Modi, M.N., Dhawale, A.K., and Bhalla, U.S. (2014). CA1 cell activity sequences emerge after reorganization of network correlation structure during associative learning. Elife *3*, e01982. https://doi.org/10.7554/eLife.01982.

35. Wu, J., Wang, R., Ye, Z., Sun, X., Chen, Z., Xia, F., Sun, Q., and Liu, L. (2015). K-Means-Based consensus clustering: a unified view. Biochem. Biophys. Res. Commun. *466*, 155–161. https://doi.org/10.1109/TKDE.2014.2316512.

36. Markus, E.J., Qin, Y.L., Leonard, B., Skaggs, W.E., McNaughton, B.L., and Barnes, C.A. (1995). Interactions between location and task affect the spatial and directional firing of hippocampal neurons. J. Neurosci. *15*, 7079–7094. https://doi.org/10.1523/JNEUROSCI.15-11-07079.1995.

37. Fenton, A.A., Lytton, W.W., Barry, J.M., Lenck-Santini, P.-P., Zinyuk, L.E., Kubík, S., Bureš, J., Poucet, B., Muller, R.U., and Olypher, A.V. (2010). Attention-like modulation of Hippocampus place cell discharge. J. Neurosci. *30*, 4613–4625. https://doi.org/10.1523/JNEUROSCI.5576-09.2010.

38. Ester, M., Kriegel, H.-P., Sander, J., and Xu, X. (1996). A density-based algorithm for discovering clusters in large spatial databases with noise. In Proceedings of the Second International Conference on Knowledge Discovery and Data Mining (AAAI Press).

39. Lopes-dos-Santos, V., Ribeiro, S., and Tort, A.B.L. (2013). Detecting cell assemblies in large neuronal populations. J. Neurosci. Methods *220*, 149–166. https://doi.org/10.1016/j.jneumeth.2013.04.010.

40. Danielson, N.B., Kaifosh, P., Zaremba, J.D., Lovett-Barron, M., Tsai, J., Denny, C.A., Balough, E.M., Goldberg, A.R., Drew, L.J., Hen, R., et al. (2016). Distinct contribution of adult-born hippocampal granule cells to context encoding. Neuron *90*, 101–112. https://doi.org/10.1016/j.neuron.2016.02.019.

41. Daigle, T.L., Madisen, L., Hage, T.A., Valley, M.T., Knoblich, U., Larsen, R.S., Takeno, M.M., Huang, L., Gu, H., Larsen, R., et al. (2018). A suite of transgenic driver and reporter mouse lines with enhanced brain-cell-type targeting and functionality. Cell *174*, 465–480.e22. https://doi.org/10.1016/j.cell.2018.06.035.

42. Bao, Y., Redington, E., Agarwal, A., and Gong, Y. (2021). Decontaminate traces from fluorescence calcium imaging videos using targeted non-negative matrix factorization. Front. Neurosci. *15*, 797421.

43. Dombeck, D.A., Harvey, C.D., Tian, L., Looger, L.L., and Tank, D.W. (2010). Functional imaging of hippocampal place cells at cellular resolution during virtual navigation. Nat. Neurosci. *13*, 1433–1440. https://doi.org/10.1038/nn.2648.

44. Muller, R.U., Kubie, J.L., and Ranck, J.B. (1987). Spatial firing patterns of hippocampal complex-spike cells in a fixed environment. J. Neurosci. *7*, 1935–1950. https://doi.org/10.1523/JNEUROSCI.07-07-01935.

45. Redish, A.D., Battaglia, F.P., Chawla, M.K., Ekstrom, A.D., Gerrard, J.L., Lipa, P., Rosenzweig, E.S., Worley, P.F., Guzowski, J.F., McNaughton, B.L., and Barnes, C.A. (2001). Independence of firing correlates of anatomically proximate hippocampal pyramidal cells. J. Neurosci. *21*, RC134. https://doi.org/10.1523/JNEUROSCI.21-05-j0004.2001.

46. Geiller, T., Sadeh, S., Rolotti, S.V., Blockus, H., Vancura, B., Negrean, A., Murray, A.J., Rózsa, B., Polleux, F., Clopath, C., and Losonczy, A. (2022). Local circuit amplification of spatial selectivity in the hippocampus. Nature *601*, 105–109. https://doi.org/10.1038/s41586-021-04169-9.

47. Hubel, D.H., and Wiesel, T.N. (1962). Receptive fields, binocular interaction and functional architecture in the cat's visual cortex. J. Physiol. *160*, 106–154. https://doi.org/10.1113/jphysiol.1962.sp006837.

48. Mountcastle, V.B. (2003). Introduction. Cerebr. Cortex *13*, 2–4. https://doi.org/10.1093/cercor/13.1.2.

49. Hampson, R.E., Simeral, J.D., and Deadwyler, S.A. (1999). Distribution of spatial and nonspatial information in dorsal hippocampus. Nature *402*, 610–614. https://doi.org/10.1038/45154.

50. Witter, M.P., Doan, T.P., Jacobsen, B., Nilssen, E.S., and Ohara, S. (2017). Architecture of the entorhinal cortex A review of entorhinal anatomy in rodents with some comparative notes. Front. Syst. Neurosci. *11*, 46.

51. Wilent, W.B., and Nitz, D.A. (2007). Discrete place fields of hippocampal formation interneurons. J. Neurophysiol. *97*, 4152–4161. https://doi.org/10.1152/jn.01200.2006.

52. English, D.F., McKenzie, S., Evans, T., Kim, K., Yoon, E., and Buzsáki, G. (2017). Pyramidal cell-interneuron circuit architecture and dynamics in hippocampal networks. Neuron *96*, 505–520.e7. https://doi.org/10.1016/j.neuron.2017.09.033.

53. Nitz, D., and McNaughton, B. (2004). Differential modulation of CA1 and dentate gyrus interneurons during exploration of novel environments. J. Neurophysiol. *91*, 863–872. https://doi.org/10.1152/jn.00614.2003.

54. Dolleman-van der Weel, M.J., Griffin, A.L., Ito, H.T., Shapiro, M.L., Witter, M.P., Vertes, R.P., and Allen, T.A. (2019). The nucleus reuniens of the thalamus sits at the nexus of a hippocampus and medial prefrontal cortex circuit enabling memory and behavior. Learn. Mem. *26*, 191–205. https://doi.org/10.1101/lm.048389.118.

55. Alexander, A.S., and Nitz, D.A. (2015). Retrosplenial cortex maps the conjunction of internal and external spaces. Nat. Neurosci. *18*, 1143–1151. https://doi.org/10.1038/nn.4058.

56. Zhang, Y., Zhang, G., Han, X., Wu, J., Li, Z., Li, X., Xiao, G., Xie, H., Fang, L., and Dai, Q. (2022). Rapid deep widefield neuron finder driven by virtual calcium imaging data. Preprint at bioRxiv. https://doi.org/10.1101/2022.01.25.474600.

57. Sun, Y., Jin, S., Lin, X., Chen, L., Qiao, X., Jiang, L., Zhou, P., Johnston, K.G., Golshani, P., Nie, Q., et al. (2019). CA1-projecting subiculum neurons facilitate object–place learning. Nat. Neurosci. *22*, 1857–1870. https://doi.org/10.1038/s41593-019-0496-y.

58. Pnevmatikakis, E.A., and Giovannucci, A. (2017). NoRMCorre: an online algorithm for piecewise rigid motion correction of calcium imaging data. J. Neurosci. Methods *291*, 83–94. https://doi.org/10.1016/j.jneumeth.2017.07.031.

59. Zhou, P., Resendez, S.L., Rodriguez-Romaguera, J., Jimenez, J.C., Neufeld, S.Q., Giovannucci, A., Friedrich, J., Pnevmatikakis, E.A., Stuber, G.D., Hen, R., et al. (2018). Efficient and accurate extraction of in vivo calcium signals from microendoscopic video data. Elife *7*, e28728. https://doi.org/10.7554/eLife.28728.

60. Friedrich, J., Zhou, P., and Paninski, L. (2017). Fast online deconvolution of calcium imaging data. PLoS Comput. Biol. *13*, e1005423. https://doi.org/10.1371/journal.pcbi.1005423.

61. Skaggs, W.E., McNaughton, B.L., Wilson, M.A., and Barnes, C.A. (1996). Theta phase precession in hippocampal neuronal populations and the compression of temporal sequences. Hippocampus *6*, 149–172. https://doi.org/10.1002/(SICI)1098-1063(1996)6:2<149::AID-HIPO6>3.0.CO;2-K.

62. Zhang, S., Schönfeld, F., Wiskott, L., and Manahan-Vaughan, D. (2014). Spatial representations of place cells in darkness are supported by path integration and border information. Front. Behav. Neurosci. *8*, 222.

STAR★METHODS

KEY RESOURCES TABLE

REAGENT or RESOURCE	SOURCE	IDENTIFIER
Bacterial and virus strains		
AAV1-CaMKII-GCaMP6f-WPRE-SV40	Addgene	100834
Chemicals, peptides, and recombinant proteins		
isoflurane	VET ONE	502017
Critical commercial assays		
bench top unit	Highland Medical Equipment	HME1-9
stereotaxic unit	Leica	Angle Two
Picospritzer	General Valve	Picospritzer III
tissue adhesive	3M	Vetbond
dental cement	Lang Dental Manufacturing	1304CLR
microtome	Leica	SM2010R
Deposited data		
calcium activity and behavior	https://data.mendeley.com/datasets/tnbwfw2pg2	https://doi.org/10.17632/tnbwfw2pg2.1
analysis code	https://github.com/xiangmixLab/Anatomical-organization-of-temporally-correlated-hippocampal-CA1-neurons/	xiangmixLab/Anatomical-organization-of-temporally-correlated-hippocampal-CA1-neurons
Experimental models: Organisms/strains		
C57BL/6J-Camk2a-Cre mice	Jackson Laboratory	000664
Ai163	Allen Institute	https://doi.org/10.1016/j.cell.2018.06.035
Camk2a-Cre	Jackson Laboratory	005396
Software and algorithms		
CNMF-E	https://github.com/zhoupc/CNMF_E	zhoupc/CNMF_E
TUnCaT	https://github.com/YijunBao/TUnCaT	YijunBao/TUnCaT
DBSCAN	https://yarpiz.com/255/ypml110-dbscan-clustering	ypml110-dbscan-clustering
GraphPad Prism 9	GraphPad Software	https://www.graphpad.com
Matlab 2017a	Mathworks	https://www.mathworks.com/
NormCorre	https://github.com/flatironinstitute/NoRMCorre	flatironinstitute/NoRMCorre
ICA-based assembly detection	https://github.com/tortlab/Cell-Assembly-Detection	tortlab/Cell-Assembly-Detection

RESOURCE AVAILABILITY

Lead contact

Further information and requests for resources and reagents should be directed to and will be fulfilled by the lead contact, Xiangmin Xu (xiangmix@hs.uci.edu).

Material availability

This study did not generate new unique reagents.

Data and code availability

- The calcium imaging data and behavior data of the study is publicly available at Mendeley data repository (Mendeley Data: https://doi.org/10.17632/tnbwfw2pg2.2) as of the date of publication, DOIs are listed in the key resources table.
- Original code used in the study is publicly available at the lab's github repository (https://github.com/xiangmixLab/Anatomical-organization-of-temporally-correlated-hippocampal-CA1-neurons). The unique identifiers are listed in the key resources table.

- Any additional information required to reanalyze the data reported in this paper is available from the lead contact upon request.

EXPERIMENTAL MODEL AND SUBJECT DETAILS

Animals

All experiments were conducted according to the National Institute of Health guidelines for animal care and use and were approved by the Institutional Animal Care and Use Committee and the Institutional Biosafety Committee of the University of California, Irvine. C57BL/6J and Camk2a-Cre mice were acquired from Jackson Laboratory for the described experiments. Ai163 mice were directly transferred from the Allen Institute for Brain Science.[41] Camk2a-Cre; Ai163 mice were obtained by crossing Ai163 and Camk2a-Cre mice. C57BL/6J and Camk2a-Cre; Ai163 mice were all between 4 and 8 months old. In the circle, square and triangle box experiment for Figures 1 and 3, 2 male and 4 female mice were included; In the open arena experiment for Figure 2 5 male and 7 female mice were included; In the linear track experiment for Figure 3 2 male and 4 female mice were included; In the barrier experiment for Figure 3 5 male mice were included; In the immobility experiment for Figure 4 3 male mice were included. Animals had access to food and water in their home cages with lights maintained on a 12 h light/dark cycle (lights on at 6:30 a.m., lights off at 6:30 p.m.).

METHOD DETAILS

Mouse surgery and viral injections

The general procedure for viral injections has been described previously.[57] To perform stereotaxic viral injections into the brain, mice were anesthetized under 1.5% isoflurane for 10 min with a 0.8 L/min oxygen flow rate using a bench top unit (HME1-9, Highland Medical Equipment). Mice were then placed into a stereotaxic unit for mice (Leica Angle Two™) with their heads secured and received continuous 1% isoflurane anesthesia. A small incision was made on the scalp and the skin was opened to expose the skull and the landmarks of bregma and lambda to determine the coordinates for the injection site. A three-axis micromanipulator guided by a digital atlas was used to determine the position of bregma and lambda. Using the micromanipulator software, the injection site was calculated relative bregma and lambda, using computerized coordinates in the digital atlas. To image *in vivo* calcium transients from CA1 excitatory neurons, 0.2ul of GCaMP6-expressing virus, AAV1-CaMKII-GCaMP6f-WPRE-SV40 (Penn Vector Core: 3.7 x 10^{13} genome copies per mL) was injected into hippocampal CA1 area (AP: −1.94 mm; ML: −1.4 mm; DV: −1.35 mm). The injection site was drilled with a small hole for the delivery of virus. 0.4ul of the GCaMP6-expressing virus was loaded into a glass pipette (tip diameter, ~20–30 μm) and delivered into target region with a Picospritzer (General Valve, Hollis, NH) at a rate of 20–30 nL/min with 10 ms pulse duration. The glass pipette was left in the brain for 5 min after injection to prevent the backflow of the virus. After the complexion of the injection, the incision of mouse was closed with tissue adhesive (3M Vetbond, St. Paul, MN). Mice were injected with 5 mg/kg Carprofen to mitigate pain and inflammation. Animals were returned to their home cage for recovery. We waited for 3 weeks after the AAV injection, which allows the infected neurons to express sufficient levels of calcium indicators. Then a follow-up procedure was performed to implant a gradient refractive index (GRIN) lens over the injection site.

GRIN lens implantation and baseplate placement

All animals were implanted with a GRIN lens at the target CA1 region for *in vivo* calcium imaging after the AAV-GCaMP injection. A 1.8-mm diameter circular craniotomy was implanted at the following coordinates of the CA1 region: AP: −2.3 mm, ML: −1.75 mm, DV: −1.55 mm. Using a scalpel to incise the skin, we removed connective tissue and dissected muscles from the edge of the skull. To enhance the stability of microscope implantation and *in vivo* imaging quality, we used a burr (Meisinger, 1/4 Round Steel) to roughen the surface of the skull and to implant a skull screw far away from the implantation area. A center point for the craniotomy was marked on the exposed skull, and surrounding this point, we etch a 1-mm radius cranial window. We carefully removed bone fragments with fine forceps and gently aspirated the exposed tissue with a 27G flat needle until seeing the white striated structure (corpus callosum) above CA1. We then changed to a 29G flat needle for tissue aspiration and stopped when the hippocampus itself was exposed. We then attached the prepared lens holder to the stereotaxic apparatus and gently lowered the GRIN lens to the target area. A small amount of krazy glue was applied around the lens within the craniotomy to cover the exposed tissue. The GRIN lens was fixed to the skull with dental cement (Lang Dental Manufacturing: 1304CLR). A thick layer of Kwik-Sil was applied to the top of the lens to protect it from

physical damages. We used a miniscope to check neural calcium activity through the GRIN lens and to adjust the placement of the baseplate for maximal neuron yields.

Open arenas experiment (ensemble activity map analysis)

After one week of handling, 12 mice were habituated in the experimental chamber for four consecutive days. The two arenas included a circular box (36 cm in diameter) and a rectangular box (32 cm*26 cm), each adorned with different distal visual cues on each wall. On the first day, animals with head-mounted miniscopes were to explore in the rectangular arena for 10 min. Then after 6 days which is generally considered sufficient for animals to forget about previous experience, animals ran in the circular arena for 10 min.

Open arenas experiment (circle, square and triangle box)

After one week of handling, 6 mice were habituated in the experimental chamber for four consecutive days. Animals with a head-mounted scope freely explored within each of three open-field arenas for 12 min. The three arenas included a circular box (36 cm in diameter), a square box (26 cm in length and width) and a triangular box (area 840 cm^2) each adorned with different visual cues on wall. In between recording sessions, the corncob bedding was changed, and the arenas were cleaned with 10% ethanol. On the first day of habituation, animals with head-mounted miniscope were first trained in the circular environments for 12 min, followed by another 12 min in the square box, and then finally they explored in the triangle box in the last 12 min. On day two, animals ran in each arena for 12 min as was done for day one, but in a different order. The actual experiments use the same design as habituation.

Barrier experiment

Camk2a-Cre; Ai 163 mice (n = 5) implanted with miniscope GRIN lenses at hippocampal CA1 were used for this experiment. Animals underwent water restriction for 1 week, given around 1 mL water per day until they reached ~80% of their original body weight. In the meantime, all animals were handled and habituated with a miniscope mounted on the head for 1 week. The recording lasted for two days with 3 sessions each day. The first day contained three training sessions in an empty square box. The second day contained three sessions, including pre-cue (empty square box), cue (square box with a black barrier positioned at the center) and post-cue (empty square box) sessions. For each session, animals were taken out from their home cage and put into a random position in the box at the beginning of the recording. The experimenter added 5-10 μL waterdrops every 30 s at a random position into the box. The water-deprived mice would search for the waterdrops across the arena. Miniscope imaging and animal behavior data were simultaneously recorded. Each session lasted for 600 s. The square box wall was painted in light gray without visual cues. Animals were able to see the surrounding environment of the room since the box wall was low. The square box had a waterproof mat on the floor. The dimensions of the square box and the barrier were 25 cm*25 cm*11 cm and 12.5 cm*12.5 cm*1.2 cm.

Linear track

6 mice were handled 5 min per day for 3 consecutive days and then trained to run on the linear track during a week of habituation sessions. Water restriction was conducted to motivate animals and the reduction of body weights was controlled within 20%. A 1-meter-long linear track made of black wood was used. 10% ethanol was used for track cleaning between each recording session. Each mouse was placed on the middle of linear track at the beginning of behavior task. The animal was required to run to the end of the track to get 10ul of water reward. Training continued until a minimum of 40 laps per session was achieved. On day 1 of the experimental recording, animals were required to go through 1 session (day 1-horizontal). On the second day, animals went through the same session as day 1 (day 2-horizontal), and then ran another 30 laps after a 90-degree rotation of the linear track relative to the recording environment (day 2-vertical). The animal was held in the experimenter's hand for a 1-min break between the two sessions.

Immobility imaging

3 mice were habituated in their home cage inside dark box for 4 consecutive days. The dark box was dimly illuminated with a blue LED. Animals' position was tracked by an Arlo wire-free camera and was used to determine the immobility periods. On the experimental day, mouse behavior and CA1 neuronal activities were first recorded with the room lights on. The animal was then placed back to the dark box (dim blue LEDs only), and imaging was made during periods of immobility for 10 min.

Histology

Mice were transcardially perfused, and the harvested brains were post-fixed in 4% paraformaldehyde overnight, followed by 30% sucrose in phosphate buffered saline for the next day. The brain was then sectioned coronally using a microtome (Leica SM2010R, 30μmslices). Brain slices near the GRIN lens implantation area of hippocampal CA1 were collected and stained with DAPI and mounted on microscope slides. Brain sections were then imaged using a fluorescence BX61 Olympus microscope to visualize fluorescently labeled (GCaMP6+) CA1 cells.

Calcium imaging data preprocessing

Calcium imaging data was downsampled to 15 frames/sec. To adjust for rigid, between-frame movements of the brain relative to the camera, motion correction was applied to the images with an established calcium imaging motion correction pipeline, NormCorre[58] (https://github.com/flatironinstitute/NoRMCorre). The corrected recordings under different conditions were aligned with each other by aligning the neurons that appeared across conditions and were combined prior to neuron extraction.

Extraction of calcium transients in individual neurons using the CNMF-E method

The calcium signals of neurons were extracted from the combined recording using the Extended Constrained Nonnegative Matrix Factorization (CNMF-E) method proposed by Zhou et al.[59] (https://github.com/zhoupc/CNMF_E). This method models the recording as follows:

$$y(\mathrm{x}, t) = \sum_{i=1}^{K} a_i(\mathrm{x}) * c_i(t) + b(\mathrm{x}, t)$$

Where $y(x, t)$ represents the raw video data, $a_i(x)$ represent the neuron's spatial footprint, $c_i(t)$ represents the temporal calcium activity and $b(x, t)$ represents the background activity. The software applies sophisticated background approximation to remove the background component, and by iteratively applying constrained nonnegative matrix factorization to the remaining data, extracts the temporal varying calcium dynamic and the spatial footprint of neurons in the recordings.

We note the footprints of CNMF-E extracted neurons usually have a bright center and gradually fade toward the periphery, while artifacts have uniform brightness or distributed bright spots. To exclude artifacts, we calculated Kullback–Leibler divergence between the footprints and a 2D normal distribution, whose peak locates at the centroid of the footprint and variance equal the variance of the footprint. The Kullback–Leibler divergence gives a value range from 0 to 1 that quantifies the similarity between two distributions, so here it represents the closeness between the actual neuron footprint and the theoretically perfect footprint. For a perfect match, the divergence value is 0. Neurons with divergence values smaller than 0.3 were kept for subsequent analyses. We also applied manual intervention to further remove false detections with aberrant shapes and temporal responses.

Mouse movement tracking

The movement trajectory of the mouse was extracted from overhead videos using a Logitech web camera which has a sample rate of 30 Hz. The floor of any given arena is selected as the region of interest (ROI) to restrict the area for detection of movement. A red LED built into the miniscope is detected inside the ROI of each frame, and its centroid position is captured using customized MATLAB software. The locomotor trajectory is constructed from the positions of red LED across all frames and smoothed with a moving average.

Autocorrelation of temporal dynamics

To quantify the time span of correlated calcium activities in temporal clusters, the calcium signals of all neurons in one cluster are added up together to get the ensemble trace, and the autocorrelation of the ensemble trace is calculated with MATLAB "xcorr" function. Half-length of the higher-than-0 autocorrelation data is considered as the time span of correlated calcium activities.

Spike train and spatial activity map calculation

For activity rate calculations, the calcium spike trains are estimated by applying the CNMF-E embedded deconvolution algorithm, OASIS,[60] to the extracted temporal calcium dynamics. A threshold of 3 times

of the standard deviation of the spike amplitudes was applied for each neuron. Spikes lower than the threshold was discarded.

Spatial activity maps were calculated as follows: the locomotor trajectory is downsampled by 2 to be aligned with the calcium responses. In all experiments, the ROI is divided into 1 cm × 1 cm bins. For each bin, the total time the mouse occupied that location is determined as is the total number of events occurring while occupying that bin (C). The spatial event rate for each bin (bin rate) is thus C/bin time. After construction, the activity map is smoothed with a 10 cm × 10 cm 2D Gaussian kernel (delta = 2 cm). This is applied to all experiments including linear track and open field arena trials. For linear track, the trajectory and calcium data within 10% of both ends were excluded as they were inside the water reward area. The number of fields was determined by counting the components inside the binarized activity maps in which only the center of the fields with bin rates higher than the 0.5 times of maximal bin rate across the map are preserved.

Ensemble activity map of each cluster was calculated by averaging the activity maps of all intra-cluster neurons.

Spatial activity map correlations

Activity maps of the same neuron in two different trials are reshaped to one-dimensional vectors, and the Pearson correlation between the reshaped vectors represents the correlation between the corresponding activity maps.

K-mean based consensus clustering (KCC) and optimal cluster numbers

We utilized a clustering method called "k-mean based consensus clustering" (KCC)[35] with slight modifications to achieve replicable clustering results while automatically determining the optimal cluster number. In detail, we first predefined a range of 2–10 as potential cluster numbers. Then for each potential number, we perform 100 rounds of k-mean clustering. In each round, neuron responses are downsampled by half, and then linearly interpolated to match the original length. K-means clustering is applied to the interpolated responses with K-means ++ seeding. Pairwise correlations between responses are used as distance for cluster calculation.

The results from 100 clustering rounds are used to build a consensus matrix that contains the pairwise similarity between neuron pairs (i.e., the number of rounds that two neurons fall into the same cluster). To determine the optimal number of clusters, we calculate the cophenetic correlation coefficient of the consensus matrixes corresponding to each of the cluster number candidates. Given a consensus matrix X, and its corresponding dendrogram of Z, the cophenetic correlation coefficient of X is calculated as follows:

$$c = \frac{\sum_{i<j}(X_{ij} - \overline{X})(Z_{ij} - \overline{Z})}{\sqrt{\sum_{i<j}(X_{ij} - \overline{X})\sum_{i<j}(Z_{ij} - \overline{Z})}}$$

Where X_{ij} is the distance between point i and j in matrix, and Z_{ij} is the dendrogram distance between point i and j. The coefficient will be higher if the hierarchical clustering result of the consensus matrix is more robust.[59] Hence, inside the predefined range, the consensus matrix with the highest cophenetic correlation corresponds to the optimal cluster number and represents the optimal clustering result.

With the optimal cluster number and its corresponding consensus matrix, hierarchical clustering is performed to the consensus matrix, and the final clustering result is defined at the hierarchical level that give the optimal number of clusters.

ICA-based clustering

We utilized the ICA-based clustering method described in previous study[39] (https://github.com/tortlab/Cell-Assembly-Detection). The method returns the weight matrix representing each neuron's contribution toward a specific assembly, and based on that, the assembly time-series can be built from the neuronal activities. For comparison with KCC-based clustering, we applied the cluster number determined by KCC-based clustering to the ICA-based algorithm. We utilize all the neurons with weight value larger than 0. For each assembly, the weights of all neurons are sorted, and a neuron will be assigned into the assembly's

neural cluster if its weight toward the current assembly is larger than that toward other assemblies. If there is a position tie between multiple assemblies, we resolve this by comparing the correlation between the neuron's transient with the assembly's activity and assign the neuron to the assembly with which it has the highest correlation.

Intra- and inter-cluster pairwise correlation and spatial distance

The pairwise Pearson correlation of calcium signals was calculated for all neuron pairs of each mouse according to their categorization as belonging to the same cluster (intra-cluster) or different clusters (inter-cluster). Baseline correlations are determined following 100 randomized shuffles of cluster identity while retaining the same number of neurons in each cluster.

For the pairwise correlation – pairwise distance data. The correlation-distance distribution was fit with a first order power function. Wilcoxon matched pair signed rank test is used to test the difference of fit curves of intra- and inter-cluster correlation-distance distribution.

Anatomically contiguous patches of CA1 anatomical space

We used Density-Based Spatial Clustering of Applications with Noise (DBSCAN)[38] to isolate the anatomically compact neuron clusters. For each neuron, DBSCAN takes its centroid and counts how many of its neighborhood neurons are within the predefined maximum neighborhood distance L. If the number of qualified neighborhood neurons are higher than the predefined number threshold N, then this neuron and its neighbors form up an anatomically compact neuron cluster. The algorithm continues to perform the same operation until no more clusters are founded and no more neurons are assigned to the existing clusters. We define L as the 95^{th} percentile of the minimum neighborhood distances for all neurons. For N, we choose an arbitrary number 3, which means the smallest anatomical cluster should have at least 3 neurons.

Having defined anatomically compact neuron groups, we define their outer boundaries by connecting the centroids of the most peripheral neurons and use the boundaries to define anatomically contiguous patches. Each cluster may have one or multiple patches. The patch size of each cluster is then calculated as the average size of all its regions. A threshold of 10% maximum patch size is applied to the calculations to minimize the influence of very small patches. To determine the chance level, we shuffle the cluster identities of neurons 100 times, and calculate the patch size for each shuffled clustering result, which formulate a distribution of patch sizes of shuffled clusters. Wilcoxon matched pair signed rank test is used to test the difference between the curves of original anatomical cluster patch size and that of averaged shuffled cluster patch size across different cluster number candidates.

Cluster overlap

Cluster overlap is quantified as the percentage of neuron pairs remaining in the same cluster across two independent clustering results. The algorithm is described as follows (Figure S1C): Suppose a group of neurons has two clustering results (in different trials for example), P1 and P2, neurons in a specific cluster c of P1 may go into N clusters in P2.

We define:a_i = number of neurons in cluster c that go into cluster i ($i = 1...N$) in P2S = total number of neurons in cluster c

Then the cluster overlap between c and the corresponding N clusters in P2 is

$$overlap = \frac{\sum_{i=1...N}\binom{a_i}{2}}{\binom{S}{2}}.$$

$\binom{a_i}{2}$ means the combinations of all possible two-neuron pairs in a population of a_i neurons. If $0 < a_i \leq 2$, $\binom{a_i}{2}$ is replaced with 1, there is only 1 possible combination of these neurons. When $a_i = 0$, $\binom{a_i}{2}$ is replaced with 0.

If P1 has M clusters, the overall cluster overlap between P1 and P2 will be the average overlap across M clusters:

$$overall\ overlap\ =\ \frac{\sum_{i\ =\ 1...M}\left(overlap_i\right)}{M}$$

The baseline for overall cluster overlap is calculated as the average of 95th percentile for 1000 shuffled overall cluster overlap for all mice.

It is noted that the difference in cluster number may affect the overlap (or non-overlap) of cluster partitions as well. To control this variability, when comparing cluster overlap between different conditions (Figure 3), we redo the clustering using a uniform cluster number for each experiment. For circle-square-triangle box, linear track and barrier experiments, the uniform cluster numbers chosen are 5, 4, 4, respectively. In Figure S3, when comparing the clusters between different periods, we first determine the cluster number using the whole 12 min data, then apply this number to all 6min periods.

Information score and place cell

Information score of recorded neurons is calculated as information per spike.[61] Only the running session with speed larger than 0.5 cm/s are included in calculation, and the spatial bins with bin time smaller than 0.1 s are excluded to avoid non-existed trespass caused by trajectory smoothing. For an activity map with n bins, the information per second is defined as:

$$Information\ Score\left(bits\ /\ spike\right)\ =\ \sum_{i\ =\ 1}^{n} P_i\frac{\lambda_i}{\lambda}log_2\frac{\lambda_i}{\lambda}$$

P_i is the probability the mouse stays in the i th bin, which is represented as the ratio between the times in the bin and total times of the trial. λ_i is the firing rate of the i th bin, while λ is the average firing rate across the trial. Place cells are defined by comparing the information score of each neuron with its shuffled baseline. All the time points along the calcium responses will be randomly shuffled for 100 times, to randomize their correspondence with behavior and generate a distribution of potential score values the neuron may achieve. A neuron is determined as a place cell if its original score value is higher than the 95th percentile of the shuffled distribution.

Spatial coherence is used to further trim the selection of place cells by the firing field smoothness. Spatial coherence is calculated as the correlation between the bin rate of each pixel and the averaged bin rate of its 8 neighboring bins.[62] Place cells with spatial coherence higher than 0.4 are selected for further analysis.

TUnCaT processing

The Temporal Unmixing of Calcium Traces (TUnCaT) software were obtained from the official github link[42] (https://github.com/YijunBao/TUnCaT). The software requires the original recording video and a mask representing the originally detected neurons. Following the TUnCaT protocol, we used the CNMF-E's neuron footprint as the neuron mask input. We used OASIS to obtain the CNMF-E like calcium trace from TUnCaT generated raw calcium traces for comparisons. We noted that TUnCaT returns empty or aberrant calcium traces for some neurons even they have acceptable CNMF-E calcium traces. We excluded these neurons from the downstream analysis. For the above-threshold peak analysis, we applied Gaussian smoothing to the signals (Gaussian window length: 6 s), as well as a threshold of 0.2 times of the maximum calcium trace amplitude to explicitly target the large activities.

QUANTIFICATION AND STATISTICAL ANALYSIS

Data are presented as the mean ± SEM. Two-tailed Wilcoxon rank-sum test was used for testing statistical significance between distributions of individual mouse. Two sample Kolmogorov-Smirnov test was used to compare the difference between cumulative distributions. Wilcoxon matched pairs signed rank test was used to test the cluster size difference across different cluster numbers, as well as to test the pairwise correlation difference across different pairwise distance. The level of statistical significance was defined as are defined as $p \leq 0.05$ *, $p < 0.01$ **, $p < 0.001$ ***. Statistical test details can be found in the corresponding legends of the figure panels.